

FABRICATION AND DOPING OF THIN CRYSTALLINE Si FILMS
PREPARED BY E-BEAM EVAPORATION ON GLASS SUBSTRATE

A THESIS SUBMITTED TO
THE GRADUATE SCHOOL OF NATURAL AND APPLIED SCIENCES
OF
MIDDLE EAST TECHNICAL UNIVERSITY

BY

SALAR HABIBPUR SEDANI

IN PARTIAL FULFILLMENT OF THE REQUIREMENTS
FOR
THE DEGREE OF MASTER OF SCIENCE
IN
MICRO AND NANOTECHNOLOGY

FEBRUARY 2013

Approval of the Thesis:

**FABRICATION AND DOPING OF THIN CRYSTALLINE Si FILMS
PREPARED BY E-BEAM EVAPORATION ON GLASS SUBSTRATE**

submitted by **SALAR HABIBPUR SEDANI** in partial fulfillment of the requirements for the degree of **Master of Science in Micro and Nanotechnology Department, Middle East Technical University** by,

Prof. Dr. Canan Özgen
Dean, Graduate School of **Natural and Applied Sciences**

Prof. Dr. Mürvet Volkan
Head of Department, **Micro and Nanotechnology**

Prof. Dr. Raşit Turan
Supervisor, **Physics Dept., METU**

Assoc. Prof. Dr. H. Emrah Ünalın
Co-Supervisor, **Metallurgical and Materials Eng., METU**

Examining Committee Members:

Prof. Dr. Mehmet Parlak
Physics Dept, METU

Prof. Dr. Raşit Turan
Physics Dept, METU

Assist. Prof. Dr. Emren Nalbant Esentürk
Chemistry Dept, METU

Assist. Prof. Dr. Kadir Ertürk
Physics Dept., Namık Kemal University

Assist. Prof. Dr. Özge Tüzün Özmen
Physics Dept., Düzce University

Date : 20.02.2013

I hereby declare that all information in this document has been obtained and presented in accordance with academic rules and ethical conduct. I also declare that, as required by these rules and conduct, I have fully cited and referenced all material and results that are not original to this work.

Name, Last Name: *SALAR HABIBPUR SEDANI*

Signature :

ABSTRACT

FABRICATION AND DOPING OF THIN CRYSTALLINE Si FILMS PREPARED BY E-BEAM EVAPORATION ON GLASS SUBSTRATE

Sedani, Salar H.

M. Sc. Department of Micro and Nanotechnology

Supervisor: Prof. Dr. Raşit Turan

Co-Supervisor: Assoc. Prof. Dr. H. Emrah Ünalın

February 2013, 55 pages

In this thesis study, fabrication and doping of silicon thin films prepared by electron beam evaporation equipped with effusion cells for solar cell applications have been investigated. Thin film amorphous Si (a-Si) layers have been fabricated by the electron beam evaporator and simultaneously doped with boron (B) and phosphorous (P) using effusion cells. Samples were prepared on glass substrates for the future solar cell operations. Following the deposition of a-Si thin film, crystallization of the films has been carried out. Solid Phase Crystallization (SPC) and Metal Induced Crystallization (MIC) have been employed to obtain thin film crystalline Si. Crystallization was performed in a conventional tube furnaces and Rapid Thermal annealing systems (RTA) as a function of process parameters such as annealing temperature and duration. Produced films have been characterized using chemical and structural characterization techniques such as Raman Spectroscopy, X-Ray Diffractometer and Secondary Ion Mass Spectrometer (SIMS). The electrical properties of the films have been studied using Hall Effect and I-V measurements as a function of doping.

We have demonstrated successful crystallization of a-Si by SPC at temperatures above 600 °C. The crystallization occurred at lower temperatures in the case of MIC. For doping, P was evaporated from the effusion cell at a temperature between 600 °C and 800 °C. For B, the evaporation temperature was 1700 °C and 1900 °C. The thickness and the band gap of the Si films were determined by ellipsometry method and the results were compared for different evaporation temperatures. The effect of doping was monitored by the I-V and Hall Effect measurements. We have seen that the doping was accomplished in most of the cases. For the samples annealed at relatively high temperatures, the measured doping type was inconsistent with the expected results. This was attributed to the contamination from the glass substrate. To understand the origin of this contamination, we analyzed the chemical structure of the film and glass by X-ray Fluorescence (XRF) and seen that the glass is the main source of contamination. In order to prevent this contamination we have suggested covering the glass substrate with Si₃N₄ (Silicon Nitride) which act as a good diffusion barrier for impurities.

Keywords: Thin Film, Crystalline, Silicon Solar Cell, Effusion Cell Equipped E-Beam Evaporator, Doping, Crystallization

ÖZ

E-BEAM BUHARLAŞTIRICIYLA CAM ÜZERİNE GÜNEŞ GÖZELERİ UYGULAMALARI İÇİN SİLİSYUM İNCE FİMLERİN ÜRETİMİ VE KATKILAMASI

Sedani, Salar H.

Yüksek Lisans, Mikro ve Nanoteknoloji Bölümü

Tez Yöneticisi: Prof. Dr. Raşit Turan

Ortak Tez Yöneticisi: Doç. Dr. H. Emrah Ünalın

Şubat 2013, 55 sayfa

Bu tez çalışmasında, efüzyon hücreleri ile donatılmış elektron demeti buharlaştırma sistemi ile hazırlanmış silisyum ince filmlerin güneş gözeleri uygulaması için üretim ve katkılanması incelenmiştir. İnce film amorf silisyum (a-Si) tabakalar elektron demeti buharlaştırıcı ile üretilmiş ve eş zamanlı olarak efüzyon hücreleri ile boron ve fosfor katkılaması yapılmıştır. Gelecekte güneş gözeleri işlemleri için ince filmler cam alttaşı üzerine üretilmiştir. A-Si ince film üretimini takiben filmlerin kristallenmesi sağlanmıştır. Kristal silisyum ince film elde etmek için, Katı Faz Kristallenme (SPC) ve Metalle İndüklemeli Kristallenme (MIC) yöntemleri kullanılmıştır. Kristallenme, klasik tüp fırınlama ve Hızlı Isıl Fırınlama (RTA) yöntemleriyle zaman ve sıcaklık değişkenlerine göre çalışılmıştır. Üretilen filmler, kimyasal ve yapısal karakterizasyon yöntemleri olan Raman spektroskopisi, X-Işını Kırınımı ve İkincil İyon Kütle Spektroskopisi (SIMS) ile incelenmiştir. Filmlerin elektriksel özellikleri katkılamanın fonksiyonu olarak Hall Etkisi ve akım-voltaj (I-V) ölçümleriyle çalışılmıştır.

600 °C sıcaklık üzerinde SPC yöntemiyle başarılı kristallenme elde edildiği gösterilmiştir. MIC durumunda kristallenme 600 °C'nin altında gözlemlenmiştir. Katkılama için efüzyon hücresinden 600 °C ve 800 °C sıcaklıkları arasında fosfor buharlaştırılmıştır. Boron için buharlaştırma sıcaklıkları 1700 °C ve 1900 °C arasında olmuştur. Filmlerin kalınlık ve bant aralıkları elipsometrik yöntemle belirlenmiş ve sonuçlar farklı buharlaştırma sıcaklıkları için karşılaştırılmıştır. Katkılamanın sonuçları I-V ve Hall etkisi ölçümleriyle gözlenmiştir. Birçok koşulda katkılamanın yapıldığı görülmüştür. Görece yüksek sıcaklıklarda fırınlanmış örneklerin katkılamanın beklenen sonuçlarla tutarlı olduğu ölçülmüştür. Bu sonuç, camdan gelen kirliliğe dayandırılmıştır. Bu kirliliğin nedenini anlamak için filmlerin ve camın kimyasal yapısı X-Işını Floresans Spektroskopisi (XRF) ile analiz edilmiş ve kirliliğin ana kaynağının cam olduğu görülmüştür. Bu kirliliği önlemek için, cam alttaşların yüzeyinin iyi bir difüzyon bariyeri olan Silisyum Nitrat (Si_3N_4) tabaka ile kaplanması öngörülmüştür.

Anahtar Kelimeler: İnce Film Kristal Silisyum, Güneş Gözesi, Efüzyon Hücresiyle Donatılmış E-Demeti Buharlaştırıcı, Katkılama, Kristallenme

*To my beloved family;
Yunes, Faeqe and Homayoon*

ACKNOWLEDGEMENTS

I would like to thank Professor Rařit Turan for his support, instructive discussions, introducing the facilities during my M.Sc education and thesis work. Also I would like to thank Assoc. Prof. Dr. Emrah Ünalın for his cooperation in studies. I am thankful to Assist. Prof. Dr. Kadir Ertürk for introducing the facilities, adapting his experience and instructive comments during this thesis work. Very special thanks to Mehmet Karaman, my dear colleague, which assist and help me in all parts of this study and to Zeynep Demirciođlu for all her aids in writing process of this thesis. Thanks to Assist. Prof. Dr. Mustafa Kulakçı for sharing his knowledge and experience. I would also like to thank Prof. Dr. Mehmet Parlak, Assist. Prof. Dr. Alpan Bek, Assoc. Prof. Dr. Burcu Akata Kurç, Assist. Prof. Dr. Ervin Tuđay, Assist. Prof. Dr. Özge Tüzün Özmen, Alper İnce, Olgu Demirciođlu, Engin Özkol, Gizem Nogay, Yasin Ergunt, Hisham Nasser, Kutlu Kutluer, Fırat Es, Yücel Eke, Serim İlday, Mete Günöven, Burcu Altuntař, Emine Hande Çiftpınar, Serra Altınoluk, Mona Zolfaghari Borra, Behzad Hosseini, Parisa Sharif, Yashar Ostovan, Negin Bagherzadi, Torkan Fazli, Farid Djavani, Melda İşler and all members of the Center for Solar Energy Resaerch and Application (*GÜNAM*) for their support and friendship. Also, for characterization and measurements, I would like to thank METU Central Lab. (MerLab).

I am thankful to my colleagues and the staffs in METU, Physics, Lab.118 for their support and understanding.

I am also thankful to my family for their endless support and confidence throughout my life.

TABLE OF CONTENTS

ABSTRACT	v
ÖZ	vi
ACKNOWLEDGEMENTS	viii
TABLE OF CONTENTS	ix
LIST OF TABLES	xi
LIST OF FIGURES.....	xii
CHAPTERS	
1. INTRODUCTION.....	1
1.1. Renewable Energies.....	1
1.2. History	2
1.3. Photovoltaic Solar Cells.....	3
1.3.1. Crystalline Silicon Photovoltaic Technology.....	3
1.3.2. a-Si Thin Film Photovoltaic Technology.....	3
1.3.3. Thin Film Crystalline Solar Cells	3
1.3.4. CIS and CIGS Solar Cells	4
1.3.5. CdTe Thin film Solar Cells.....	4
1.3.6. Dye Sensitized Solar Cells (DSSC)	4
1.3.7. Organic Solar Cells	4
1.4. Principles of PV solar cell	4
1.5. Solar Radiation	9
1.6. Organization of The Thesis.....	10
2. THIN FILM CRYSTALLINE Si FOR SOLAR CELL APPLICATIONS	11
2.1. Introduction to Thin Film Modules.....	11
2.2. Fabrication of Thin Crystalline Si Film	12
2.2.1. Fabrication by Chemical Vapor Deposition (CVD).....	12
2.2.2. Fabrication by Sputtering	14
2.2.3. Fabrication by e-beam Evaporation	14
2.3. Thin Film Solar Cell (p-i-n).....	15
2.3.1. a-Si and $\mu\text{c-Si:H}$ based thin film solar cells.....	15
2.3.2. Thin Film Crystalline Si Solar Cell.....	16
2.4. Metal Induced Crystallization.....	16
2.5. Modeling of Crystallization.....	17
3. EXPERIMENTAL PROCEDURES FOR FABRICATION AND CHARACTERIZATION OF CRYSTALLINE Si THIN FILMS	19
3.1. Electron Beam Evaporator System with Effusion Cells	19
3.2. Selection of Substrate.....	21
3.2.1. Substrate Cleaning.....	22

3.3. Deposition Process of a-Si and involved Effective Parameters	22
3.3.1. Substrate Temperature	22
3.3.2. Deposition Rate	22
3.3.3. Effect of e-beam Spot Size (Current Density)	22
3.3.4. Film Thickness	23
3.4. Doping.....	23
3.4.1. Boron Effusion Cell.....	23
3.4.2. Phosphorous Effusion Cell	24
3.5. Crystallization by Solid-Phase Crystallization (SPC).....	24
3.5.1. SPC by Annealing in Standard Furnace	24
3.5.2. SPC by Rapid Temperature Annealing (RTA)	24
3.6. Metal Induced Crystallization (MIC).....	25
3.6.1. Metal Coating Process for Metal Induced Studies	25
3.6.2. Metal Induced Crystallization by Au Nanoparticles (AuNPs)	26
3.8. Characterization and Measurement Techniques.....	27
3.8.1. I-V Measurements (current vs. voltage)	27
3.8.2. Hall Effect Measurements	27
3.8.3. Time-of-Flight Secondary Ion Mass Spectroscopy	29
3.8.4. Scanning Electron Microscopy (SEM).....	30
3.8.5. Raman Spectroscopy	30
3.8.6. X-Ray Diffraction Measurement (XRD)	31
4. RESULTS AND DISCUSSION	33
4.1. Crystallization of a-Si Thin Films Prepared by e-beam Evaporation	33
4.1.1. Solid-Phase Crystallization (SPC).....	33
4.1.2. Metal Induced Crystallization by Au Nanoparticles (AuNPs)	39
4.2. Doping a-Si Thin Film Deposited by e-beam Evaporation.....	43
4.2.1. SIMS Results.....	43
4.2.2. Electrical measurements	45
4.2.3. Activation energy measurement.....	47
4.3. Contamination from the glass substrate	48
4.3.1. SIMS Results.....	48
4.3.2. XRF Results	49
5. CONCLUSIONS.....	51
REFERENCES.....	53

LIST OF TABLES

TABLES

Table 2.1 <i>A comparison of popular thin film deposition technologies</i>	14
Table 4.1 <i>Naming the sample through conditions on deposition rate, thickness and RTA temperature</i>	35
Table 4.2 <i>Crystallinity amounts of AuNPs induced samples with respect to different annealing temperature and time</i>	42
Table 4.3 <i>Effusion cells' temperature survey study table</i>	43
Table 4.4 <i>Hall Effect measurements for B-doped samples with different effusion cell temperatures</i>	46
Table 4.5 <i>Hall Effect measurements for P-doped samples with different effusion cell temperatures</i>	46

LIST OF FIGURES

FIGURES

Figure 1.1 Total energy demands with respect to countries [1].....	1
Figure 1.2 Cross section of a p-n junction device, charge distribution, electric field, electric potential.....	5
Figure 1.3 Characteristics of a p-n junction under dark (a) and illuminated (b) conditions	6
Figure 1.4 Standard I-V curves with I_{sc} , V_{oc} and power terms	6
Figure 1.5 Fill Factor (FF) trough the I-V curve.....	7
Figure 1.6 Various semi-conductors bandgap overlap with solar spectrum for AM0 and AM1.5 [14].....	9
Figure 1.7 Definitions of the AM0, AM1.5 and many others from the National Department of Energy [15].....	9
Figure 2.1 Structure of a-Si thin film through Solid-Phase Crystallization [26].....	12
Figure 2.2 (a) Schematic view of sputtering process and (b) Sputter deposition chamber ...	14
Figure 2.3 (a) Single junction amorphous and micromorph solar cell, (b) Spectral response of micromorph solar cell [40].....	15
Figure 2.4 A typical solar cell based on thin film crystalline Si [45]	16
Figure 2.5 Schematic of ALILE process. The layer stack before (left) and after (right) the layer exchange are shown. The oxide interface layer remains in position during the process	17
Figure 2.6 Diagram of the Kolmogorov-Johnson-Mehl-Avrami equation. The fraction RC of the new phase is plotted as a function of time [62].....	18
Figure 3.1 Simple portrait of electron gone action	19
Figure 3.2 Electron Beam Evaporator System at GÜNAM	20
Figure 3.3 (a) Pure silicon pieces, (b) pure boron pieces, (c) gallium phosphide cube	20
Figure 3.4 Schematic illustration of the modified PBN crucible	21
Figure 3.5 Schott BOROFLOAT® 33 chemical compositions [64].....	22
Figure 3.6 Systematic plot of an effusion cell a) inner Parts, b) cooling system	23
Figure 3.7 Scheme of standard furnace with temperature gradient.....	24
Figure 3.8 Schematics of a RTA furnace	25
Figure 3.9 Schematics of the thermal evaporator	25
Figure 3.10 Simple schematic of AuNPs induced a-Si crystallization process.....	26
Figure 3.11 Shadow masks for a)I-V measurements b)Hall effect measurements by van der Pauw technique.....	26
Figure 3.12 Schematics for I-V measurements.....	27
Figure 3.13 Hall Effect Measurement System (for an assumed n-type semiconductor)	28
Figure 3.14 Hall Effect voltage vs. van der Pauw resistance measurement configurations. .	29
Figure 3.15 Representation of SIMS experiment. Primary beam removes substrate atoms from the surface.	29
Figure 3.16 Systematics of the ToF-SIMS systems of METU Central Laboratory [65]	30
Figure 3.17 Shift up and down in Raman Spectra [66].....	31
Figure 3.18 Schematics of the X-Ray Diffraction experiment.....	32
Figure 4.1 Study of a-Si model sample [500 nm thick, 10 A/s deposited on AF32®eco glass substrate at 200 °C] annealed at 750 °C in different time whiles	34
Figure 4.2 Crystallinity changes vs. annealing time.....	35
Figure 4.3. Crystallization study by getting deposition rate as only variable in 800 °C-10min annealing case.....	36
Figure 4.4 Crystallization study by getting deposition rate as only variable in 800 °C-15min annealing case (5 min more).....	36
Figure 4.5 Comparison of thickness and deposition rate effect on crystallization amount; a) 20 A/s & 500 nm, b) 5 A/s & 500 nm, c) 20 A/s & 250 nm and d) 5 A/s & 250 nm.....	37

Figure 4.6 Study of a-Si model sample [500nm thick, 10 Å/s deposited on 400nm AZO coated AF32 [®] eco glass substrate at 200 °C] annealed at 750 °C in different time whiles...	38
Figure 4.7 Comparison of two spot shape results in 650 °C annealing for 1 h which is a kind of threshold annealing for 1000nm 50Å/s deposited a-Si sample	39
Figure 4.8 SEM images of 15 nm gold thin film after annealing at 500 °C for 1 hour	40
Figure 4.9 Raman measurements for samples of 1 µm - 1 Å/s a-Si with AuNPs on AZO/glass substrate annealed for 12 h at 500 °C, 550 °C and 600 °C	40
Figure 4.10 XRD measurements for samples of 1 µm - 1 Å/s a-Si with AuNPs on AZO/glass substrate annealed for 12 h at 500 °C, 550 °C and 600 °C, also at 600 °C for 0 h, 3 h, 12 h	41
Figure 4.11 Effect study of AuNPs for case of 600 °C annealing for 12 h	42
Figure 4.12 SIMS result of B doping in effusion cell's different temperatures	44
Figure 4.13 SIMS result of P doping in effusion cell's different temperatures	44
Figure 4.14 I-V curve for Boron doping of different effusion cell temperatures	45
Figure 4.15 I-V curve for Phosphorous doping of different effusion cell's temperatures	45
Figure 4.16 Activation energy measurement for B-doped sample	47
Figure 4.17 Activation energy measurement for p-doped sample	47
Figure 4.18 SIMS result to comparison Al, Ca, Fe and Na impurities in a-Si film	49
Figure 4.19 XRF Results.....	50

CHAPTER 1

INTRODUCTION

1.1. Renewable Energies

Energy is not just a scientific, technological or economical term; it's a case that rules the world. It has economical, social and environmental effects on our life on this planet. As known, we have been using fossil originated fuel sources to supply our energy needs. Burning fossil fuels creates enormous economical, political, and environmental problems like global warming which is becoming more and more difficult to handle.

The energy demand of human being is increasing with ever increasing rate. This unavoidable and irreversible process should be handled with extreme care in order to prevent deadly catastrophes on our planet. The expected increase in the energy demand is illustrated in Figure 1.1.

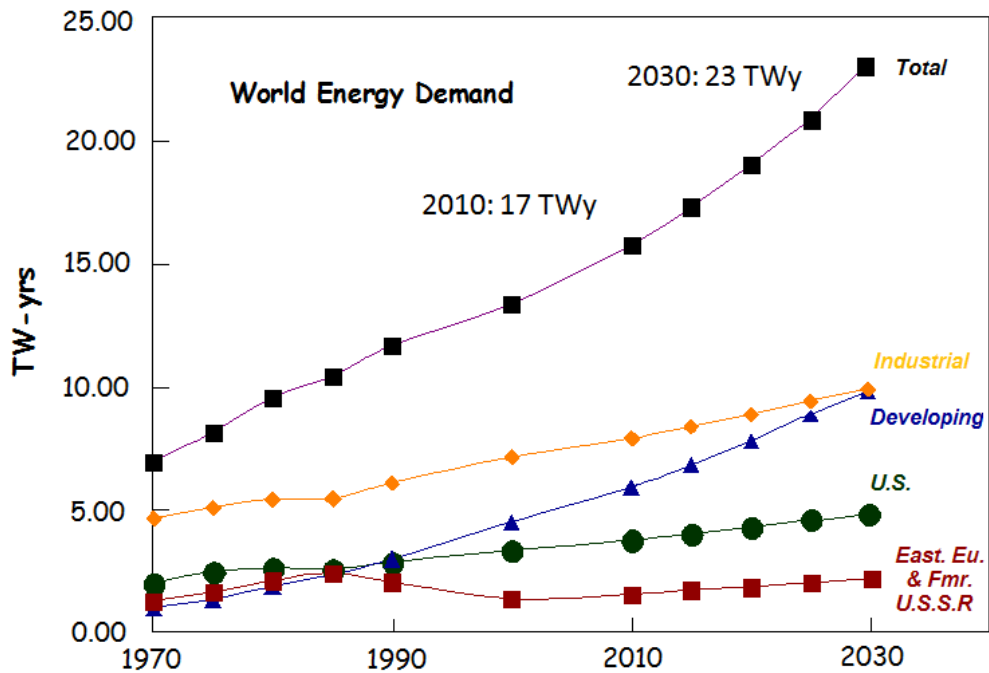


Figure 1.1 Total energy demands with respect to countries [1]

We see from Figure 1.1 that the energy demand will increase 40%, from 17 TWy to 23 TWy in 20 years. This means we have to build new huge amount of power stations in a very short time period. Today, almost 85% of the energy need is supplied by fossil fuels, coal, oil, and natural gas. Burning these fuels causes huge amount of CO₂ release to the atmosphere. This is threatening the natural life on the planet.

We certainly need to replace the fossil fuels by renewable energy resources. The major renewable energy sources are the wind power, solar power, geothermal, hydro power, wave power and biomass. Among them, solar power is the most manageable one due to being much more abundant on the planet Earth. Sun radiates 380×10^{21} kW energy while the Earth receives 170×10^{12} kW portion of it which is a huge amount of energy [2]. Photovoltaic energy is the conversion of solar power into electricity. In this process there is no toxicity, waste products and also it doesn't need any mechanically moving parts. It works where the solar or artificial light source is available (even in cloudy weather), and can be modular, can be sized for any application from a watch to a multi-megawatt power plant. But also it includes disadvantages or literally some limitations as; fully dependent on to the light. It has high initial costs that overshadow the low maintenance costs and lack of fuel costs and large area is essential for large scale applications. It also generates direct current while the electricity grid uses alternative current and at last, in off-grid applications energy storage is needed.

The main challenge about this PV technology has been the cost until very recently. The drastic price fall due to the over capacity created by China and Far East countries has made the PV applications very competitive against other energy resources. However, further price reduction is needed to create a paradigm shift from the world of fossil fuels to solar based energy world. The cost reduction can be accelerated using less materials in the photovoltaic cells. The thin film a-Si based solar cell is a promising example for the use of less material in a solar cell. However a-Si suffers from low material quality and instability. a-Si named as cheap because of its cost and its quality as a photovoltaic material. It is highly defected such include enormous amount of dangling bonds. But it is possible to change "cheap" word to "low cost" by crystallizing it. This sentence is going to be explained more in this chapter as followed.

1.2. History

French physicist, Alexandre-Edmond Becquerel (1820-1891), discovered the photovoltaic effect in 1839. He had investigated the photochemical effects of solar radiation [3]. Latterly, Edward Weston (1850-1936), an English chemist whom had been competitor of Thomas Edison in the early days of electricity generation and distribution. He was awarded a patent for the solar cell in 1882 [4]. Albert Einstein explained the photoelectric effect in 1905 which brought him a Nobel Prize in 1921 [5]. After 25 years later, in 1946, the first practical solar cell with 6 % efficiency was achieved at Bell Laboratories by Daryl Chapin, Calvin Souther Fuller and Gerald Pearson [6]. In 1958 solar cells were used to supply some portion of energy necessity of spacecraft Vanguard I to extend the mission time [7].

However the high cost of producing solar cells was an obstacle for practical use. In 1960s when the production of larger crystal ingots was available after the semiconductor industry's movement to integrated circuits, the prices became relatively lower. However this was not enough for serial production and at the beginning of 70s the costs were surmised as \$100 per watt [8]. From early 70s to the mid 80s the photovoltaic installations grew rapidly however the falling oil prices in 80s retarded the photovoltaic progress until 1996. By the end of 90s photovoltaic developments accelerated due to the green house effect problem [9]. The productions were mostly dominant in North America and Europe until 2000s. When the Asian countries, especially China, became a part of production, the prices have fallen down effectively. In 2011, it was reported that the price per watt for crystalline based solar modules was \$ 1.09[10]. After 2000 the photovoltaic growth developed consistently and large capacity solar power plants were constructed. Photovoltaic production has increased

about 40 % every year and at the end of 2010 the installed capacity reached 39.8 GW [11]. This number increased to 69 GW in the early 2012 [12].

1.3. Photovoltaic Solar Cells

Over the last 30 years, various photovoltaic technologies have been developed for solar energy conversion. While crystalline silicon solar cells are still main technology in the PV market, thin film technologies, and other third generation are also promising for future of PV technologies. Some of the new technologies have been commercialized and some of them are still in research labs and waiting for further developments.

1.3.1. Crystalline Silicon Photovoltaic Technology

Crystalline silicon cells made of bulk Si wafers and dominate market by more than %90 of the total sales. This technology is based on the well-known semiconductor, Si which is reliable and robust and has high conversion efficiency. The initial investment is low and the volume of production has reached very high level in recent years. Crystalline silicon PV cells are divided in to sub groups based on the crystallinity of the wafer: mono-crystal and multi crystal. Mono-crystalline wafer based solar cells have better quality and higher efficiency compared to the multi-crystalline ones. Multi crystalline wafers consist of different crystalline domains with different crystal orientation. This technology has low production cost that makes it competitive to the mono crystalline wafer systems.

The crystalline Si systems have reached very mature level. The cost of these systems is becoming more and more competitive. However, thin film based technologies are still a strong alternative to the bulk crystalline technologies because of cost and production advantages.

1.3.2. a-Si Thin Film Photovoltaic Technology

Thin film silicon solar cells fabricated on glass or flexible substrates has been an important alternative to other technologies due to the cost and production advantages. They can be produced in an integrated way, meaning that all production steps can be done in a single line in the same facility. The size can be very large. Up to 5.7 m² modules have been produced in recent years. Although the initial investment is high, the cost of these systems can be low compared to crystalline solar cells. The major disadvantage is however, the low efficiency in these systems. The low efficiency is partly due to the low material quality and partly due to the low material thickness that lowers the light absorption. In these systems, a p-i-n structure is used instead of a single p-n junction that is used in the crystalline solar cells.

1.3.3. Thin Film Crystalline Solar Cells

One obvious method to improve the material quality of the a-Si thin film system is to crystallize the a-Si thin film used in the cell. To replace the a-Si active layer with the crystalline, many research groups and commercial companies have carried out research projects and activities. The electrical parameters of the thin film such as resistivity, electron mobility are improved with the crystallization. Crystalline Si thin film is the main topics of this study. The problems related to the fabrication of high quality thin films are the most important issue to be investigated

Although, many successful device realizations have been reported recently, the efficiency of the solar cells produced with the thin film crystalline Si has been low (around 10%). Once high efficiency values (like 15) have been achieved, this technology will have significant impact on the present PV industry. For this purpose, new approaches and technology improvements are necessary for the next generation crystalline Si solar cells.

1.3.4. CIS and CIGS Solar Cells

Like a-Si solar cells, thin film photovoltaic devices based on other technologies have been developed. CIS (Copper Indium Selenide) and CIGS (Copper Indium Gallium Selenide) solar cells are another class of thin film solar cells which have attracted a lot of attention both academically and commercially. Today the highest efficiency thin film solar cells in the market are CIGS solar cells. Having a direct band gap, CIGS has a high absorption coefficient than other system. In addition, since CIGS solar cells can be deposited on flexible substrates, leading to new application areas in the PV technologies.

1.3.5. CdTe Thin film Solar Cells

Another thin film system is based CdTe material. Low cost and high solar absorption with 1.5 eV bandgap makes it a popular for commercial applications in the world market. Today, the production volume of CdTe solar cells reached very high values. CdTe solar cells consist of CdTe substrate and CdS emitter layer to create p-n junction.

1.3.6. Dye Sensitized Solar Cells (DSSC)

Dye Sensitized Solar Cell consists of combination of dye molecules with a wide band gap material like TiO₂. With very easy production method and low costs, DSSC has been studied very intensively in recent years. It is possible to make them semi-transparent and colorful. So, DSSC technology can find applications in applications with esthetic properties. Reasonably high efficiency values (up to 11%) have been demonstrated. These advantages have led to commercialization. One of the drawbacks of his technology is the use of liquid material and the need for a good sealing. These properties are not desirable for a product which is expected to be durable for 25 years.

1.3.7. Organic Solar Cells

In organic solar cells, polymers are used to convert the solar radiation in to electricity. Although they have problems like light induced degradation, it is a promising technology for the future of photovoltaic industry. There are different types of organic device designs with different polymer materials. Main problem about organic solar cells are low quantum efficiency and instability problems of the materials.

1.4. Principles of PV solar cell

In a PV solar cells, semiconductor materials are used to generate electron and hole flow. A photon gives its energy to a valance electron and excites it to upper level while leaving behind a lack of an electron that is known as a hole. A semiconductor having more electrons are called n-type semiconductor, while the one with more holes is called a p-type semiconductor. If an n-type and p-type semiconductor is connected to each other, a p-n junction is formed. A p-n junction is the basic device structure in today's microelectronics and solar cell industry. Schematics of a p-n junction, the electric field, electric potential and charge distributions are given in Figure 1.2.

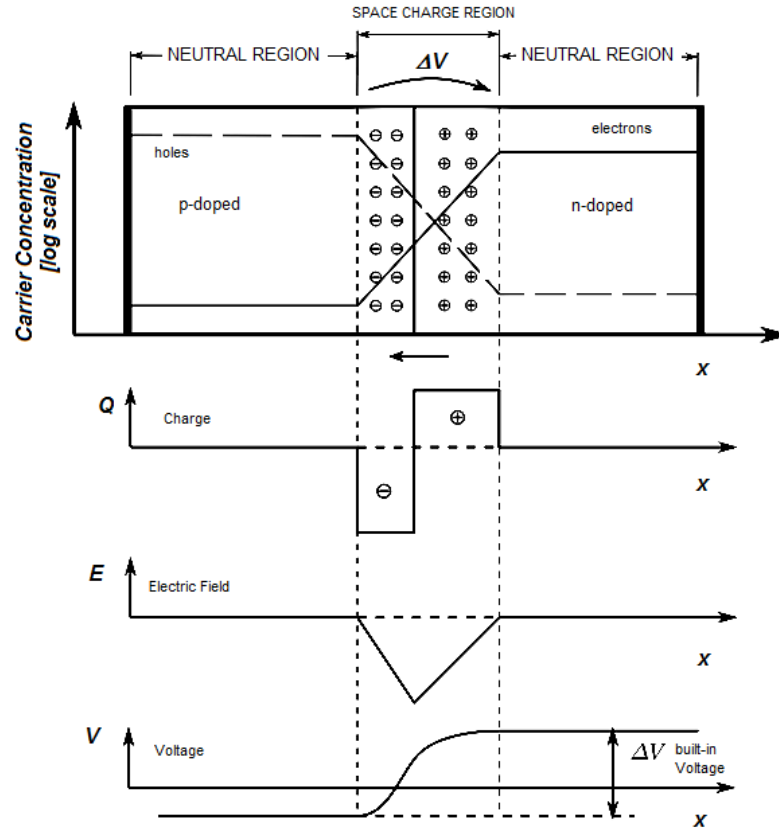


Figure 1.2 Cross section of a p-n junction device, charge distribution, electric field, electric potential

A regular p-n junction under dark condition works according to the ordinary diode equation;

$$I = I_0 \left(e^{\frac{qV}{kT}} - 1 \right) \quad (1.1)$$

where I is the current flowing through the device under the applied bias V . I_0 is the dark saturation current, q is the electric charge, k is the Boltzmann constant and T is the absolute temperature. Under dark, when the voltage is applied as forward bias the barrier between n and p type region is reduced and the majority carriers (electrons) in n type start to diffuse to p type region and holes flow to the opposite side. However there are minority carriers in both regions. Minority carriers can be excited by any extra energy like heat, light and it is independent from the applied bias. In a conventional p-n junction diode the dark saturation current is explained by minority carriers which move to opposite direction with respect to majority carriers. When the diode is illuminated, the number of minority carriers increases and the electric field at the junction passes the minority carriers to the other side. When this contribution is added, the equation 1.1 becomes;

$$I = I_0 \left(e^{\frac{qV}{kT}} - 1 \right) - I_L \quad (1.2)$$

where I_L is the contribution of illumination, in other words the current generation by the light. Schematically the dark and illuminated diode is given in Figure 1.3 *Characteristics of a p-n junction under dark (a) and illuminated (b) conditions* Figure 1.3 .

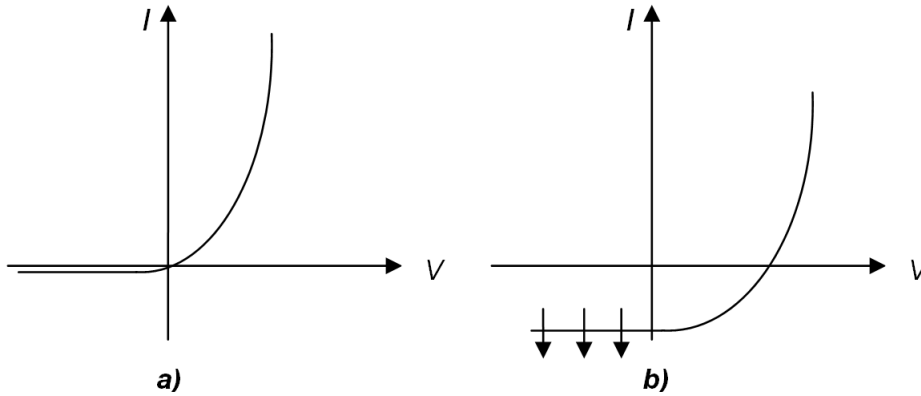


Figure 1.3 Characteristics of a p-n junction under dark (a) and illuminated (b) conditions

In solar cell operation, technically the fourth quadrant of illuminated diode is used and for simplicity it is represented by the mirrored version which is given in Figure 1.4. Below the most important parameters are described;

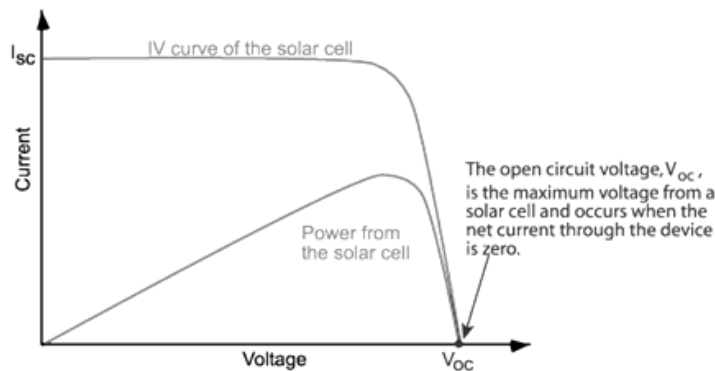


Figure 1.4 Standard I-V curves with I_{sc} , V_{oc} and power terms

Short-Circuit Current (I_{sc}); The short circuit current is the current value measured when the voltage across the junction is zero. It is determined by the light generated electrons and holes. It is a measure of how much current can be collected from a solar cell when there is no load in the circuit. In an ideal solar cell the short circuit current is equal to the collected current. Short circuit current is affected by the amount of generated minority carriers. The light and material interaction has an important role in current generation, so, reflection, absorption and photon flux are the distinctive parameters.

Open-Circuit Voltage (V_{oc}); The voltage measured when $I = 0$ is called Open-Circuit Voltage (V_{oc}). There is a correspondence between open-circuit voltage value and the short circuit voltage. The expression giving this correspondence is give below.

$$V_{oc} = \frac{nkT}{q} \ln \frac{I_{sc}}{I_0} + 1 \quad (1.3)$$

Open-circuit voltage would not expect to have large variations for a given material system because it is determined by the band gap and built in potential of the junction.

Fill Factor (FF); The short-circuit current is an extreme value for the amount of current that can be generated in a solar cell. The maximum power that can be generated by a solar cell is found by plotting I vs. V as shown in Figure 1.4. The maximum of this curve is not located at $I = 0$, it is at some point closer to V_{oc} .

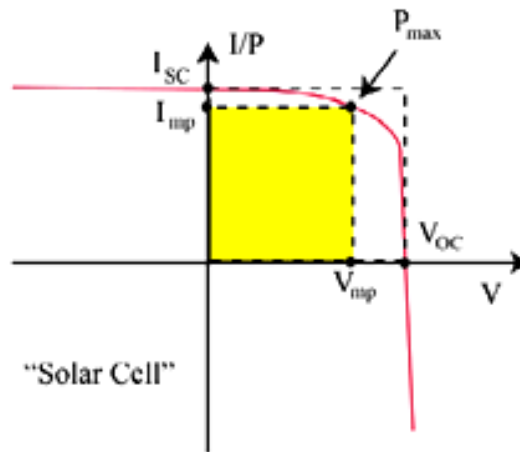


Figure 1.5 Fill Factor (FF) through the I-V curve

The Fill Factor (FF) is defined as the ratio of the maximum power from the solar cell to the product of V_{oc} and I_{sc} . It can be also seen as a measure of the *squareness* of the IV curve. FF is given as a percentage value and is a measure of the ideality of a solar cell.

The FF can be calculated from the maximum power point where the derivative of the I-V curve is zero,

$$\frac{d(IV)}{dV} = 0 \quad (1.4)$$

The FF is then found from the relation given below [13]

$$FF = \frac{V_{MP} I_{MP}}{V_{oc} I_{sc}} \quad (1.5)$$

The maximum power that can be extracted from a solar cell is then given as

$$P_{max} = V_{oc} I_{sc} FF \quad (1.6)$$

Efficiency (η); Literally, efficiency is one of the most used and important parameter to make comparisons between the performances of the solar cells. In all solar cell systems the ratio of the output power to input power is defined as the efficiency

$$\eta = \frac{P_{max}}{P_{in}} = \frac{V_{oc}I_{sc}FF}{P_{in}} \quad (1.7)$$

The efficiency of the solar cell depends on environmental conditions such as the medium temperature, the intensity of incoming light and incident sunlight's spectrum.

It is obvious that for all realistic systems there is no ideal solar cell with 100% efficiency. This is due to the limits in the energy conversion.

There exist two major limitations in the energy conversion: *Thermodynamic Limit*, and *Bandgap-Sunlight Spectrum Limit*. The latter one is due to the use of single band gap material in the solar cells system.

Thermodynamic Limit; Generation of electricity can be assumed to be a Carnot process whose efficiency is given as

$$Carnot\ Efficiency = \frac{T_{sun} - T_{earth}}{T_{sun}} = 95 \quad (1.8)$$

It is important to know that, this value is an absolute upper limit. However, the thermodynamic limit is reduced towards 85 % because of unavoidable losses of entropy. This value is valid only the limitation due to the band gap is not present, i.e., valid only there is an infinite stack of p- n junctions with all possible bandgap values.

Bandgap-Sunlight Spectrum Limit; A semiconductor can convert photons to an electrical current only when the photon energy exceeds the band gap of the semiconductor. Otherwise, photons are not absorbed by the semiconductor. On the other hand, a single photon can generate only one electron–hole pair no matter how high its energy is. The excess energy that a photon might be carrying is lost as heat in the semiconductor. So, both in the ultraviolet and infrared parts of the spectrum, significant amount of energy is lost due to this limitation in a single band gap solar cell. In order to remove this limitation, multijunction solar cells have been developed and produced. Currently, triple junction GaAs solar cells have reached record efficiency value exceeding 44%.

When we add all limitation effects, we reach an absolute efficiency value for a single junction solar cell. This limit as a function of the band gap of the material for various sun radiations is shown in Figure 1.6. We see that the maximum efficiency does not exceed 30% for all material systems. It can be seen that both crystalline and amorphous silicon are not at the maximum but relatively close to it.

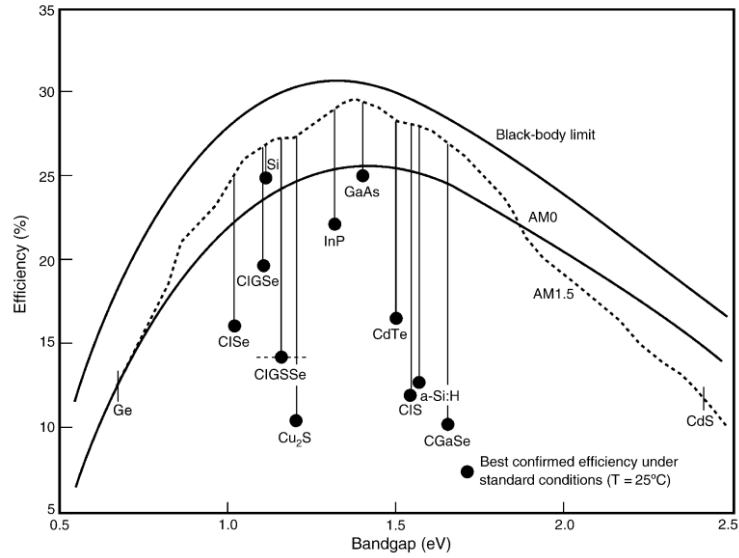


Figure 1.6 Various semi-conductors bandgap overlap with solar spectrum for AM0 and AM1.5 [13]

1.5. Solar Radiation

As a black body having a surface temperature of 6000 K, the sun generate enormous amount of energy continuously. The power generated on the surface of the sun is 63 MW/m². The solar radiation reaching just outside of the earth's atmosphere is about 1300 W/m². The effects of the absorption in the atmosphere are seen in Figure 1.7. We see that several absorption bands exist in the solar spectrum reaching the surface of the earth. These bands are due to the absorption mostly by CO₂ and H₂O in the atmosphere.

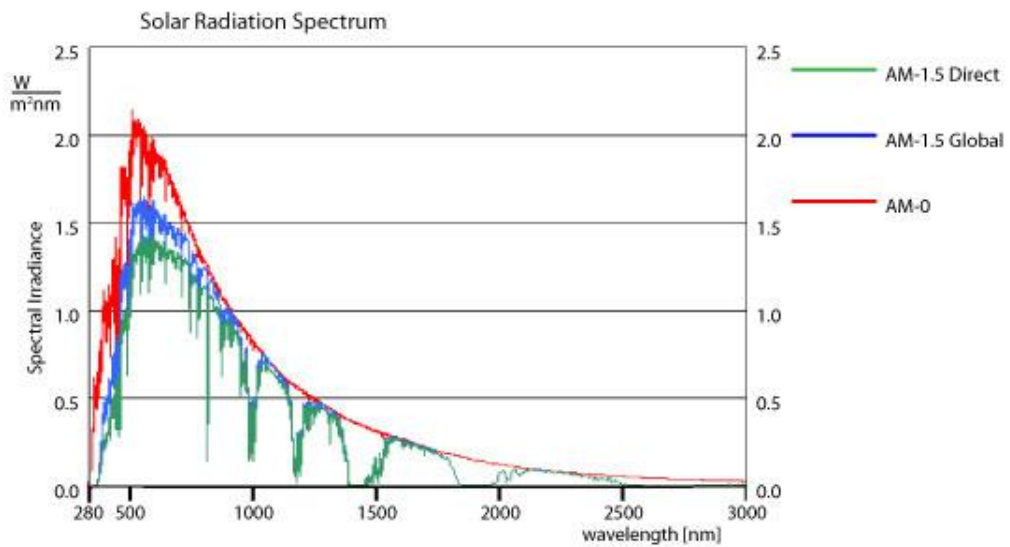


Figure 1.7 Definitions of the AM0, AM1.5 and many others from the National Department of Energy [15]

Definition of AM1.5; We need some standards for the evaluation of the cells and the worldwide testing of a solar cell is done with respect to Air Mass concept. Air Mass is the measure of absorbed light while passing through the atmosphere. Air Mass 0 states the power just on the outer surface of atmosphere which corresponds to 1353 W/m^2 and when the light enters the atmosphere the power of light decreases according to the optical path that it takes. Air mass 1 represents the power on the sea level when the sun is just ahead. Solar cells are mostly measured according to the accepted value of Air Mass 1.5 which corresponds to the power on the sea level when the sun has an angle of 48.2° with respect to Air Mass 1 condition [16]. This optical path length results in a power of approximately 1000 W/m^2 Simply Air mass is calculated by the equation;

$$\text{Air Mass} = 1/\cos(\theta) \quad (1.9)$$

where θ represents the angle of sun.

1.6. Organization of The Thesis

This thesis is organized as 4 chapters. In Chapter 1, we present an introduction the solar energy and photovoltaic solar cells. Chapter 2 introduces thin film crystalline Si for solar cell application through global research and techniques. Chapter 3 explains the fabrication process and the used measurement techniques. At last, in Chapter 4 it is discussed the results and fulfill this study aims.

CHAPTER 2

THIN FILM CRYSTALLINE Si FOR SOLAR CELL APPLICATIONS

2.1. Introduction to Thin Film Modules

Most of nowadays photovoltaic (PV) modules are produced by crystalline silicon (c-Si) based cells. The market share of the c-Si technology exceeds 85% [17]. There are many reasons for the dominance of c-Si cells in current market.

One of the main reasons is the high module efficiency which stands in 15–19% range. Another reason is that c-Si solar cells are robust and produced by reliable fabrication processes. Additionally, they have an excellent long-term stability which could reach more than 25 years. Also, the raw material is abundant and nontoxic. It should also be noted that Si technology has been developed through extensive research and development efforts in the integrated circuit (IC) industry. So, knowledge and methodology have already been accumulated to a great extent.

However, the major problem has been the silicon wafers cost. Almost 50% of the cost of a standard PV module using mono and multi-crystalline Si wafers is due to the cost of the Si wafer. If the aim is to reach values below $1\$/W_p$ for a competitive PV industry, one should reduce the cost of the used material. In this direction, the most promising approach is to use thin-film technologies in which less raw material are used. Generally, thin film concepts are considered second generation photovoltaics [18]. They are usually fabricated on glass substrates. It is also possible to make them on stainless steel and flexible substrates. Today, they hold about 10% of the total PV market. However, the low material cost is balanced with a low efficiency in these systems. The efficiency of a-Si based solar cells is around 10% which is almost half of the c-Si solar cells.

The dilemma of low efficiency-high material cost can be overcome with another approach which combines the advantages of c-Si and a-Si thin film technologies. In this case, if crystalline Si can be fabricated as a thin film on an inexpensive substrate like glass or stainless steel, high efficiency and low cost could be obtained in the same system. Recently, there has been significant amount of effort have been devoted to obtain thin crystalline Si film on glass substrate [19]-24]. In most of these studies, an a-Si thin film is first deposited on glass and then crystallized using a thermal treatment. Different approaches have been employed to obtain best material as device properties.

The most important problem in this process is the limitation of process temperatures. For the case of standard glass, it has strain points at about 600°C that restricts all process comparatively to low margins. One needs to achieve the crystallization at a temperature equal to or lower than 600 °C.

Thin film crystalline Si has partly been used in the microcrystalline silicon (μ c-Si) modules. In this case μ c-Si obtained even below 200 °C which leads to the efficiencies to above 10 % [25]. As an example, tandem modules with two p-i-n junction based on μ c-Si:H/a-Si:H cells

approaches an initial efficiencies of 13.5 % [25]. $\mu\text{-Si}$ is obtained during the deposition of Si thin film by PECVD. The crystallization is highly dependent of the hydrogen amount in the gas, and the film thickness. The structure of the film produced by a PECVD is schematically shown in Figure 2.1. We see that crystallization is initiated only after certain thickness is reached for a certain amount of hydrogen gas in the plasma.

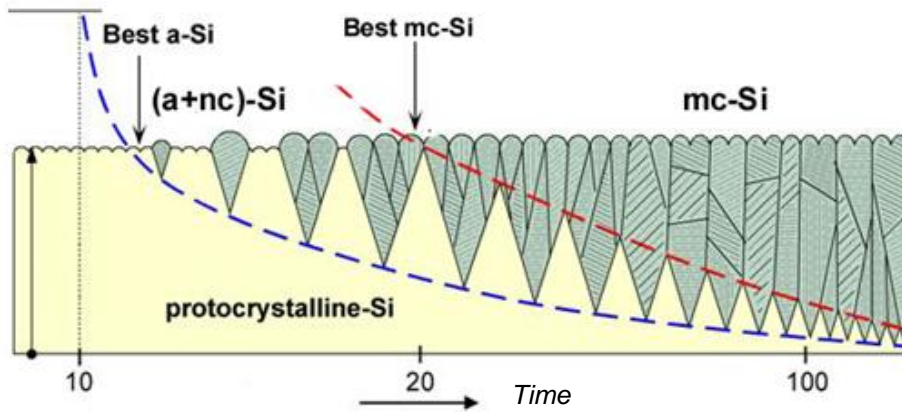


Figure 2.1 Structure of a-Si thin film through Solid-Phase Crystallization [26]

However, with small crystalline grains, $\mu\text{-Si}$ thin films are not true crystalline Si with high electrical quality. One should obtain large crystalline grains to reach the electrical properties of crystalline Si. For this purpose, we need to develop new crystallization procedures. Grained size exceeding the film thickness is essential to reach the required material properties. It has been shown that, large grain sizes can be achieved using so called Solid Phase Crystallization (SPC). However, as mentioned above, one needs a heat treatment at 600°C or above at which the low cost glass substrates start to soften. In order to overcome this problem and lower the crystallization temperatures, new crystallization techniques have been investigated. One of the promising approaches is to employ Metal Induced Crystallization (MIC) in which metals are brought to be in contact with amorphous silicon. In this case, metals act as catalyst and induce the crystallization at a lower temperature. However, the price that we pay for this low temperature crystallization is the high recombination rates in the solar cells.

In this chapter we summarize the basic features of the thin film crystalline Si.

2.2. Fabrication of Thin Crystalline Si Film

There are various techniques to be employed to fabricate thin crystalline Si film on a substrate on glass. Each technique has advantage and disadvantages. Chemical Vapor Deposition (CVD) technique is efficient but expensive and limited. Sputtering is a low temperature technique but produces low quality material. At last, fabrication by E-beam evaporation would be employed which is the main technique used in this study. E beam evaporation is a low cost and highly efficient technique for the thin film production.

2.2.1. Fabrication by Chemical Vapor Deposition (CVD)

Deposition of silicon by CVD is a costly and complex method. In this deposition technique, a precursor and dilutant gas are used to induce a chemical reaction that leads to the

deposition of Si thin film on a substrate. In conventional CVDs, high temperatures (higher than 900 °C) are needed to induce the chemical reactions. In the case of Plasma Enhanced Chemical Vapor Deposition (PECVD) the chemical decomposition is achieved by an electromagnetic agitation applied externally. In this case, the reaction takes place at low temperatures.

There are different types of CVD systems for thin film depositions. Some of them are shortly described below.

Atmospheric pressure CVD (APCVD) is based on mass transport controlled system, which allows access of gases to the substrate surfaces with a low packing density configuration. In case of low pressure CVD (LPCVD) deposition, the dominant regime is kinetically controlled. It allows high packing density. However, deposition rates are generally lower for the LPCVD systems.. The crystallinity degree obtained with LPCVD depends critically on the temperature. A complete crystalline film could be achievable at around 580~620°C. It is obvious below this temperature range may result as partly crystalline or amorphous Si films [27],[28]. In the case of LPCVD, pressures change in the range 1~100 Pa. In comparison of deposition rates, LPCVD act just one order of magnitude lower at similar temperatures.

Rapid thermal CVD (RTCVD) is another type of CVD which has been established at Fraunhofer ISE with employing an optically-heated APCVD system [29]. As Carrier, a special quartz wafer is employed which hold two layers of wafers on it.

Large grain sizes make LPCVD as a suitable technique to thin film silicon deposition on foreign substrates [16]. Also, it is able to coat large substrates [30],[31]. In comparison of poly-Si product of LPCVD with poly-Si formed at low temperatures by plasma enhanced CVD (PECVD) and RF sputtering, the Hall mobility results higher while strain inside grains is lower [30]. Of course, handling a large amount of substrates with keeping uniformity, even capability of in-situ doping and reasonably low level of surface damage make LPCVD advantageous than PECVD or sputtering techniques [31].

PECVD has several advantages) [32]. The plasma activation increases the rate of deposition even at low temperatures. Hereby, chemical bonds breaking energy is provided by the plasma, which allows deposition at temperatures as low as 200~300°C. Systematically, dissociation of the gas molecules is accomplished by high energy electrons in the plasma which make the chemical reaction accelerated. Additionally, positive ions from the plasma bombardment the substrate surface which may change the surface chemistry which might affect the product's structure and growth rate [33].

In PECVDs, substrates are either downstream or within the plasma which restricts the number of products in a simultaneous process. PECVD may help out with in-situ hydrogenization which includes hydrogen content about 10% of atomic amount [31]. Low hydrogen content is so useful which suppress spontaneous nucleation during deposition. Therefore, temperatures of about 500C are used to avoid bubble creation on substrate [31].

One of the common techniques is Hot-Wire CVD (HWCVD) technique, in which source gases such as SiH₄ and H₂ are pyrolytically decomposed on filament catalyser. This is achieved by heating the gas stream up to 1300 ~ 2000 °C at a location state several centimeters from the surface of the substrates. Adding a mixture of B₂H₆ or PH₃ into the source gas could do the doping process [34]. Generally, HWCVD technique would be known as a simple and low cost procedure[34][35]. It demonstrates single step fabrication for poly-Si [35] and reasonable deposition rates with achievable good doping control [36][38]. Superposition of precursors is the critical point which if it is optimized the large area deposition may be achievable by a multiple filament equipped system [37].

2.2.2. Fabrication by Sputtering

Sputtering is a simple technique which employs highly energetic ions that eject atoms from a target. Ejected atoms from the target are then deposited on a substrate. This technique is based on the momentum transfer between the energetic ions and source atoms. The sputtering is done in a vacuum chamber which is evacuated to about $10^{-6} \sim 10^{-7}$ Torr. Ar atoms ionized by a high voltage arc method are accelerated towards the negatively biased target. These accelerated ions hit the target and as a result sputter the source atoms. The sputtered atoms form a thin film on substrate and surroundings. (Figure 2.2)

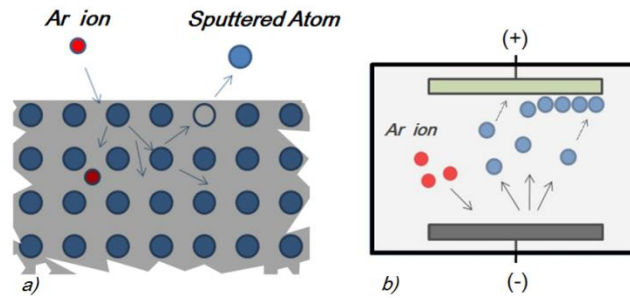


Figure 2.2 (a) Schematic view of sputtering process and (b) Sputter deposition chamber

2.2.3. Fabrication by e-beam Evaporation

In this thesis study, we have used e-beam evaporation technique to produce thin a-Si films on glass substrates. A more detailed description of this technique is given in the next chapter. In this section, a comparison of e-beam evaporation technique with other popular thin film deposition methods is provided and shown in Table 2.1 (partially referred to Ref. [Ohring2001]). Three-beam evaporation has higher deposition rates and lower impurity levels in comparison with thermal evaporation. The higher source temperature of the e-beam evaporation yields higher deposition rates. In thermal evaporation systems, the crucible itself heats up and may let impurities to diffuse into the deposited thin film.

Table 2.1 A comparison of popular thin film deposition technologies

Deposition method	Deposition rate (nm/min)	Impurity level	Uniformity	Film density	Directionality	Cost
Thermal evaporation	5 – 100	High	Poor	Low	High	Low
E-beam evaporation	50 – 1k	Low	Poor	Low	High	Medium
Sputtering	< ~ 150	Medium	Good	High	Low	Medium
PECVD	< 60	Very Low	Good	High	Low	High

The e-beam evaporation is a clean and non toxic process. In all CVD based systems toxic or flammable gases (SiH_4 and B_2H_5 , PH_3) are used for film deposition and doping. It does not suffer from the ion damage problem which is one of the major problems in the sputtering systems. The e-beam evaporation system presents also the following advantages: (1) it provides uniformity on large substrate areas; (2) it has high directionality; (3) it has high deposition rate.

The major disadvantages of the e-beam evaporation technique are: stoichiometrical difference between the source material and the deposited film if a compound evaporant is used, and (4) low adatom mobility.

2.3. Thin Film Solar Cell (p-i-n)

2.3.1. a-Si and $\mu\text{c-Si:H}$ based thin film solar cells

In this section we describe the thin film solar cells made of a-Si or c-Si thin films. In these applications, a p-i-n structure shown in Figure 2.3 is commonly used. The use of p-i-n diode instead of a single p-n junction is due to the increased absorption in the relatively thick intrinsic layer sandwiched between p and n layer.

Amorphous silicon (a-Si:H) work is a low cost material which is easily produced by one of the techniques described above. Due to its direct band gap structure, it has high absorption coefficient. For this reason, a-Si:H with 500nm of thickness is enough to construct a solar cell, because it has higher absorption coefficient than c-Si. It can be fabricated on any substrates like glass, metals or flexible materials. A single junction a-Si:H p-i-n module could reach to 9.5% efficiency [39]. This low production cost would attract market by its providence.

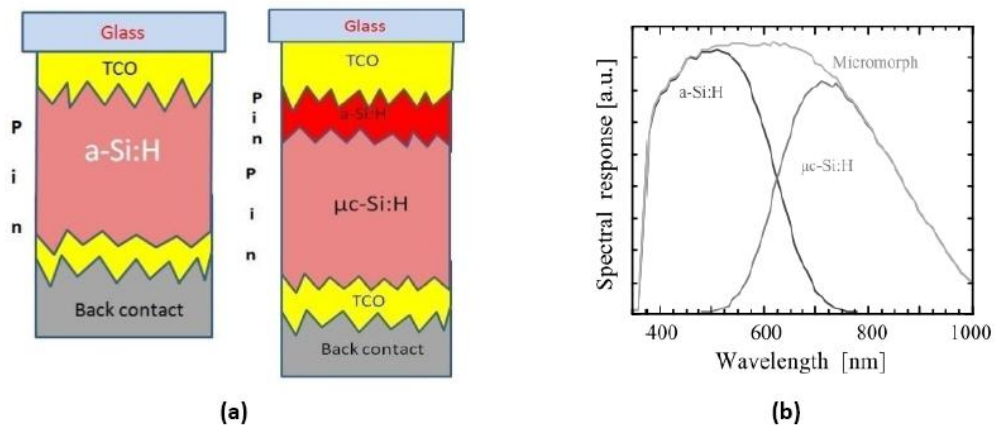


Figure 2.3 (a) Single junction amorphous and micromorph solar cell, (b) Spectral response of micromorph solar cell [40]

The efficiency improvement has been achieved using more than one junction which is called tandem solar cell. This concept comes true by making absorption from a wider solar spectrum. It consists of at least two type of p-i-n structures stacked on each other (Figure 2.3.a). Hereby, an a-Si:H p-i-n structure is placed on microcrystalline silicon ($\mu\text{c-Si:H}$) p-i-n. Two cells are complementary with two different band gap values of 1.7 eV for a-Si and 1.12

eV for $\mu\text{-Si:H}$, which provides sensitivity to corresponding portions of the solar spectrum. The a-Si:H cell harvest higher energy photons and let lower energy photons reach underlying $\mu\text{-Si:H}$ layer. This inevitably result inefficiency improvement (Figure 2.3.b). Hence, a-Si:H harvest higher energy photons and let lower energy photons as infrared ones to reach and absorb to $\mu\text{-Si:H}$ layer. The cell efficiency values are recently recorded to be 11.9% [41].

2.3.2. Thin Film Crystalline Si Solar Cell

As explained in the next chapter, the use of crystalline Si in thin film solar cell would improve electrical properties of the thin film. This is because of increased life time, increased carrier mobility, and higher conductivity in the film. These improvements are expected to result in higher efficiency in the solar cell. A typical crystalline Si thin film solar cell is schematically shown in Figure 2.4. Here, all layers of the cell are made of poly crystalline Si fabricated by solid phase crystallization technique.

The cell performance reported so far is still far from the desired values. The best reported cell efficiency value is 10.4% for this type of solar cells [42]. However, the advantage of use of crystalline Si in thin film systems is very clear and solution of the problems related to the material properties will bring the efficiency to higher values. It is therefore highly interesting to pursue research programs on this material system.

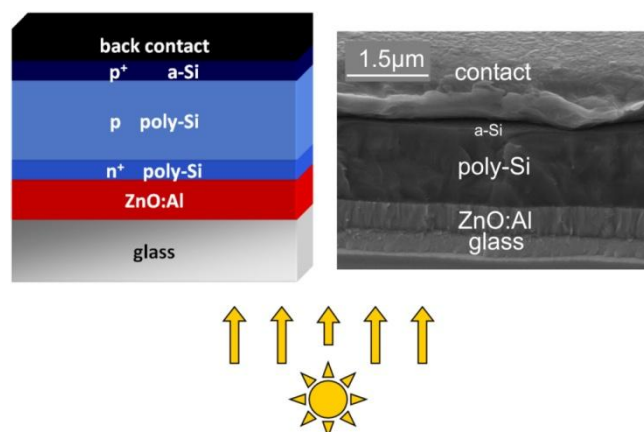


Figure 2.4 A typical solar cell based on thin film crystalline Si [43]

2.4. Metal Induced Crystallization

As discussed in the following chapter more specifically, high process temperatures needed for crystallization makes it impossible or impractical to use ordinary glass substrate. We need new approaches to reduce the process temperature and crystallization time. One of the new techniques employed for this purpose is based on the Metal Induced Crystallization (MIC) [44]. MIC is a low cost and simpler technique than others such as flash lamp annealing [45] and laser annealing proposed for the fabrication of thin crystalline films on glass at low ambient temperatures [46]. Metals like Al, Au, and Ni behave as a catalyst when used in contact with silicon [47]. Different metal types result in different crystallization characteristics which also depend on the annealing temperature and time [48]. It is commonly accepted that the crystallization starts at the metal/Si interface or the growth of crystalline structures continues by a thermal diffusion process.

Aluminum Induced Crystallization (AIC) was introduced in 1998 by O. Nast et al [49]. It is also known as aluminum induced layer exchange process (ALILE). Literally this process occurs as exchange of positions between aluminum and an amorphous silicon bi-layer. This whole story begins and ends on a glass substrate. As product a smooth, continuous and features large grains ($> 10 \mu\text{m}$) polycrystalline of silicon layer would appear [50]. This result has a preferential (100) as orientation. Therefore, ALILE layers got as seed layer which is a template for maintain low temperature epitaxy. The exchange process of ALILE is shown schematically in Figure 2.4.

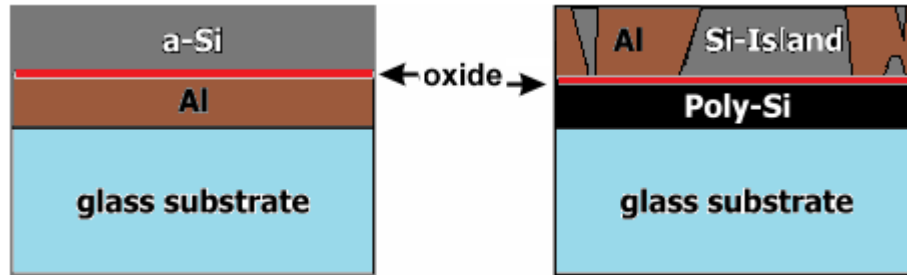


Figure 2.5 Schematic of ALILE process. The layer stack before (left) and after (right) the layer exchange are shown. The oxide interface layer remains in position during the process

The primary glass/Al/oxide/a-Si module (left side) is transformed to a glass/poly-Si/oxide/Al(+Si) mode (right side). Logically, the primary a-Si layer ought to be thicker than the primary Al layer to get continuum of poly-Si layer production. The surplus Si got remains within Al layer as c-Si islands. The key point of this process is to employ an interlayer of Al and a-Si. Commonly a natural Al-oxide layer let to be formed on top of the Al layer before the a-Si deposition. It acts as a membrane and let an exchange process which result as crystallized silicon underneath of this occasion.

Gold (Au) Induced Crystallization (GIC) is another novel approach which is one of the topics studied in this study. As a further improvement, we have studied the use of Au nanoparticles instead of continuous thin film. The amount of metal and thus the metal related contamination is reduced in this way.

As known, in the presence of a metal inclusion, the crystallization starts at lower temperatures[51][52] which Au seems to pursue such a different path in comparison with other metals. Prior experiments and the theory of this composite system predict that the Au/a-Si system forms a metastable phase Au_3Si phase which show up at very low temperature of 100°C [53].The crystallization of Si is then accomplished by the decomposition of this metastable system at relatively low temperatures. It is reported that the crystallization temperature of Au induced hydrogenated amorphous silicon is around 500°C [54].

2.5. Modeling of Crystallization

The reduction of the Gibbs energy force drives the crystallization process. For the description of the kinetics of phase changes the Gibbs energy is reduced per atom transferred from phase I (amorphous) to phase II (crystalline). But at the same time an interface between both phases has to be formed. The formation of this interface requires energy and thus increases the Gibbs energy of the system. While the Gibbs energy

reduction per atom due to the phase transition is proportional to the number of atoms in the new phase, i.e. the volume, the interface energy is proportional to the surface area of the new phase.

The KJMA-model (Kolmogorov, Johnson, Mehl, Avrami) describe theoretically the kinetics of phase change. The model based on the assumption of the *germ nuclei* existence which leads to growth nuclei at a certain nucleation rate. The phase transition gets into a certain growth rate. In addition, the model considers the geometrical restrictions for the growing grains by either neighboring grains or surfaces of the system. The KJMA model fulfilled with a characteristic functional equation. This functional equation named later as the Kolmogorov-Johnson-Mehl-Avrami equation, because of the contributions of all four authors (A.E. Kolmogorov [55], W.A. Johnson and R.F. Mehl [56] and M. Avrami[57][58][59]). The time dependent fraction of the new phase $R_C(t)$ within the volume under investigation can be written as:

$$R_C(t) = 1 - \exp(-At^m) \quad (2.1)$$

A is a nucleation- and growth rate-dependent constant and m characterizes the experimental conditions and dimension of the growing nuclei. The nucleation rate and radius growth rate of the nuclei are assumed to be constant. The formation energy of a surface can be drastically decrease by already existing surfaces. A reduction of both, critical radius and activation energy to form a nucleus accompanied reduction of this surface energy.

This is a so effective case, thus homogenous and heterogeneous nucleations are distinguished, without and with already existing surfaces, respectively. The most probable heterogeneous nucleation sites complement to the *germ nuclei* of the KJMA-model. In Figure 2.6 R_C is plotted versus time t. Here, $R_C = 0$ coincides to the initial phase before the process starts and $R_C = 1$ designates the transformation of the entire volume. As the first nucleation passed, the new phase fraction R_C increases superlinearly because new growth nuclei are formed and the transformed volume increases with larger grains due to the constant radius growth velocity. Growth limited with the slope of R_C decreases which means neighboring growth nuclei collide and the nucleation ends. The KJMA model [60] and the theory of nucleation and growth during phase separation are still state of discussion [61].

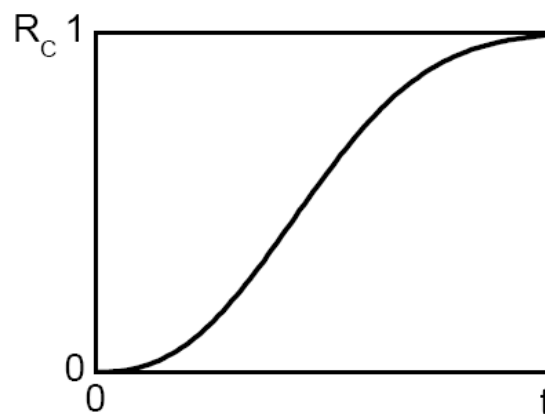


Figure 2.6 Diagram of the Kolmogorov-Johnson-Mehl-Avrami equation. The fraction R_C of the new phase is plotted as a function of time [62]

CHAPTER 3

EXPERIMENTAL PROCEDURES FOR FABRICATION AND CHARACTERIZATION OF CRYSTALLINE Si THIN FILMS

In this chapter we summarize the experimental procedures for the production of Si thin films fabricated by e-beam evaporation. We describe technical details and working principles of e-beam evaporation system equipped with effusion cells for doping, and the principles of test and measurement systems used for the characterization of the deposited films.

3.1. Electron Beam Evaporator System with Effusion Cells

In an electron beam evaporation system, the target material (Si pieces in crucible) is heated by an electron beam created by a filament source. The electron beam is accelerated and focused on to the target material with an electromagnetic field created by a static magnet and an electrostatic electric field generator. This setup is schematically shown in Figure 3.1. The evaporation process should be carried out in a vacuum chamber with a high vacuum level ($\sim 10^{-6} - 10^{-7}$).

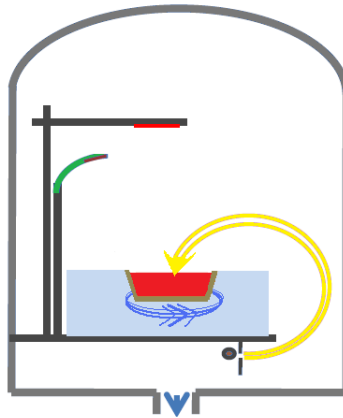


Figure 3.1 Simple portrait of electron gone action

The e-beam evaporation system available at *Center for Solar Energy Research and Applications (GÜNAM)* facility is schematically shown in Figure 3.2. This system is uniquely designed and produced by a vacuum system manufacturer Vaksis in Turkey.

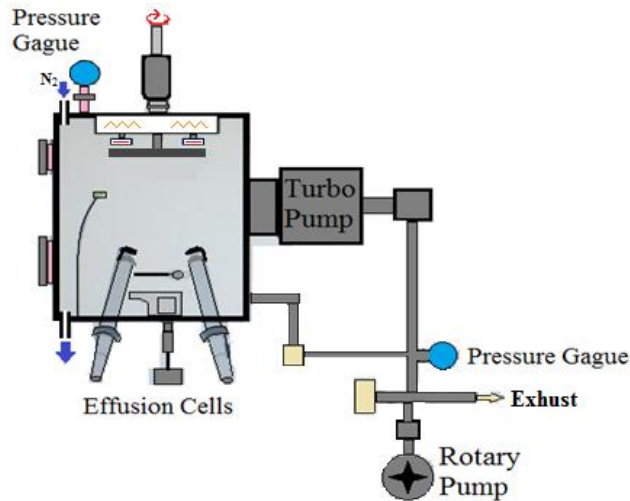


Figure 3.2 *Electron Beam Evaporator System at GÜNAM*

Here, in addition to the e-beam evaporator, the system has two effusion cells for boron (B) and phosphorous (P) doping. While doping is done using pure B source the P doping is obtain using gallium phosphide (GaP) compound. The advantage of this system is that effusion cells enable direct addition of dopants' vapor to main flux of silicon beam. Photographs of source materials used for Si evaporation, B and P doping are shown in Figure 3.3.



Figure 3.3 (a) *Pure silicon pieces*, (b) *pure boron pieces*, (c) *gallium phosphide cube*

Boron doping is simply accomplished by direct evaporation. In the case of P doping, the phosphorous atoms is extracted from the sublimation of phosphorus from GaP. The separation of parasitic Ga atoms from the GaP beam is done efficiently using a special pyrolytic boron nitride (PBN) orifice plate system which is mounted on the top of the pyrolytic BN crucible as shown in Figure 3.4. PBN has a good thermal conductivity, high insulation resistance, and high dielectric strength over wide temperature range. BN orifice acts as a powerful trap for the Ga atoms.

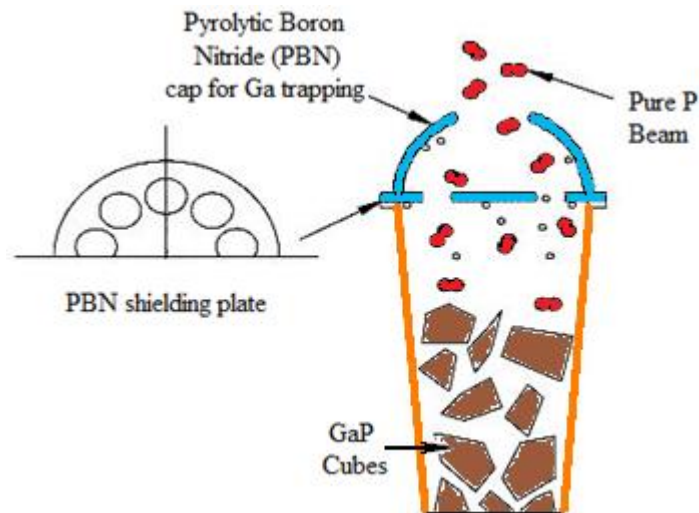


Figure 3.4 Schematic illustration of the modified PBN crucible

3.2. Selection of Substrate

The substrate for thin film deposition is glass, which is low cost and appropriate for thin film Si technology applications. During the evaporation, the substrate is placed on a sample holder located above the three-beam evaporation system. Two different glass types were selected in this study. The first one was the Schott thin glass type, AF32[®] eco which is an aluminoborosilicate glass produced without using refining agents (arsenic and antimony), using the down-draw technology process that enables production in very thin thicknesses between 0.1 and 1.1 mm. It is alkali-free in synthesis; however, contents of alkali oxide up to 0.2 weight percentages are possible by contamination of the raw materials and refractory material. It is preferred for its coefficient of thermal expansion which matches to silicon, high temperature resistance and high transmission that make it a perfect choice for this study aim [63].

Second glass type used in this study is Schott's BOROFLOAT[®] 33, which is a clear and transparent colorless glass. Its excellent transmission and very weak fluorescence intensities over the entire light spectrum make BOROFLOAT[®] 33 ideal for a wide range of optical applications such as photovoltaic technologies which employ the glass for various purposes. BOROFLOAT[®] 33, type glass has a high overall transmission for ultraviolet, visible and infrared wavelengths. It has low alkali content; BOROFLOAT[®] 33 works as a good electric insulator [64]. The chemical composition of this glass type is shown in Figure 3.5. This amount of B and Al (aluminum) may cause pollution of sample.

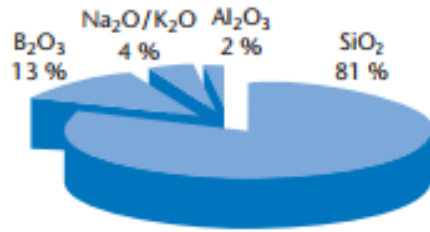


Figure 3.5 Schott BOROFLOAT® 33 chemical compositions [64]

In some cases, we used Si as substrate for calibration and characterization purposes. For example, to trace some contaminating elements such as Al and B that can be originated from the glass substrate, we have processed glass and Si (as reference) substrates under identical conditions and measured the impurity content in the film. Likewise in some cases, quartz substrate would be useful for the optimization of the crystallization.

3.2.1. Substrate Cleaning

Cleaning is a simple but critical step for a good material output. Glass substrates used in this study were cleaned using a series of washing and chemical processes that includes sonication in pure acetone, isopropanol and deionized water respectively for 20 min per each. Sometimes, glass substrates were exposed to acid/base cleaning method. In this method, substrates were first sonicated for 20 min in 0.1 molar sodium hydroxide (NaOH) solution followed by sonicating in deionized water. In the second step, then they are cleaned in a 0.1 molar hydrochloric acid (HCl) solution washed in deionized water again. Afterwards, substrates are dried by N₂ gas flow.

For Si wafer cleaning, which was used as a reference, an additional hydrofluoric acid (HF) etching would be beneficial for silicon oxide removal, which is an essential step before crystallization. It is done by simply dipping of sample in 0.3 molar HF solution for 3-10 seconds.

3.3. Deposition Process of a-Si and involved Effective Parameters

The process parameters of a-Si deposition are summarized in this chapter

3.3.1. Substrate Temperature

The system has a pair of ceramic covered heaters that are located behind the stainless steel substrate holder. Samples could be heated up during deposition. The substrate temperature can reach 200 °C.

3.3.2. Deposition Rate

The rate of deposition is an important parameter. It is controlled by the amount of e-beam current used to heat the target material. The rate of deposition can be controlled within the range of 1 nm/sec to 50 nm/sec. As will be presented in the next chapter, the rate of deposition has very important consequences in the crystallization process. The electron gun was fixed at 8.5 kV during the evaporation process. There were two process variables that affect the deposition process: e-beam current density and the spot size. The e-beam current can be as high as 230 mA.

3.3.3. Effect of e-beam Spot Size (Current Density)

The properties of the evaporated films were expected to be influenced by the size of the spot falling on the target material. In order to get the same flux, one needs to apply higher

amount of current for the smaller spot sizes. This leads to a higher kinetic energy for the evaporated atoms for the smaller spot sizes.

3.3.4. Film Thickness

For p-i-n solar cell fabrication, one needs to deposit a film with total thickness of 1-2 μm . This thickness is required for a sufficient absorption of solar radiation. This thickness can be reached only with sufficiently high deposition rates.

3.4. Doping

Doping is a very critical process for the solar cell production. One needs to create p and n type materials for p-i-n formation. As explained previously, effusion cells were used in this work for B and P doping for p-type and n-type material production.

3.4.1. Boron Effusion Cell

Effusion cells have generally a heater part, which operates with DC electrical power and shielding parts. (Figure 3.6 (a)).

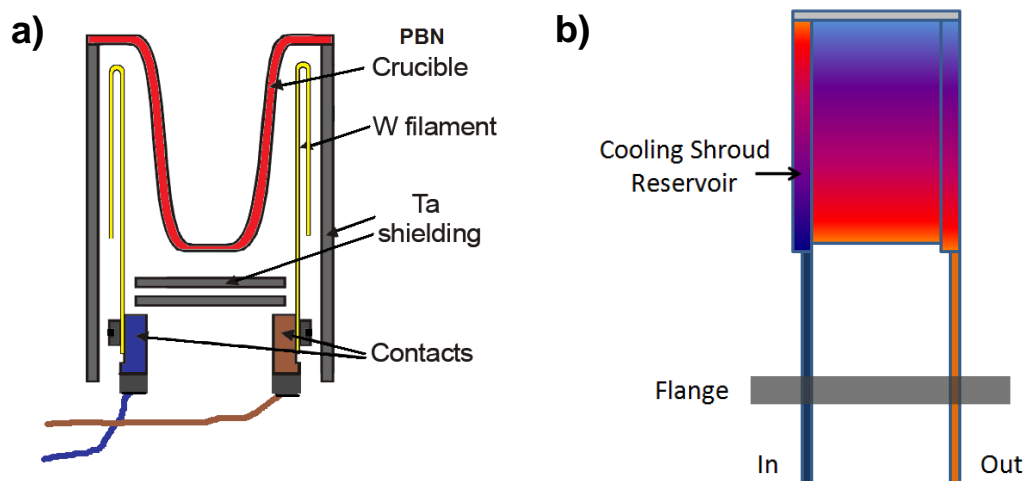


Figure 3.6 Systematic plot of an effusion cell a) inner Parts, b) cooling system

Generally, effusion cells are designed for efficient operation in the temperature range of 600-1200°C. Due to their highly efficient heat shielding produced by tantalum (Ta) and PBN shields, they control temperature very precisely. In addition, a cooling system surrounding the cell unit provides good insulation between the cell and the vacuum chamber (Figure 3.6 (b)).

Pure B has a melting point of 2079°C. However, under high vacuum conditions, the sublimation starts to occur at lower temperatures. For this reason, the B effusion cell was controlled in the temperature range of 1600-1900 °C.

3.4.2. Phosphorous Effusion Cell

As discussed previously, GaP was used to obtain pure P. Pure P can not be used because it is explosive and also it has a low sublimation temperature making it difficult to control the flux. In order to extract P from GaP compound, a Ga trap was used as shown in Figure 3.4. Temperature range for the GaP evaporation was 600-800°C.

3.5. Crystallization by Solid-Phase Crystallization (SPC)

Solid-phase crystallization (SPC) is a simple technique to fabricate crystalline thin film from amorphous phase.

3.5.1. SPC by Annealing in Standard Furnace

In standard furnaces, there is a tube which is heated up by resistive coils. For passivation of the annealing environment a high purity nitrogen gas is flowed through the system (Figure 3.7).

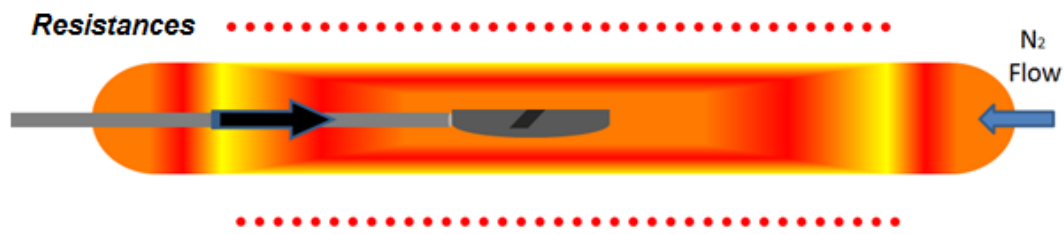


Figure 3.7 Scheme of standard furnace with temperature gradient

The temperature of the furnace can be set to desired value. The sample is placed in a quartz boat that is loaded into the tube furnace. The loading time and the annealing duration can be manually adjusted.

3.5.2. SPC by Rapid Temperature Annealing (RTA)

This type of furnace can be rapidly heated to the desired temperature using high power halogen lamps, as seen in Figure 3.8. The temperature of the sample can be increased up to 1100°C in a few seconds. For this rapid heating process, the chamber size is usually made small compared to the conventional furnaces.

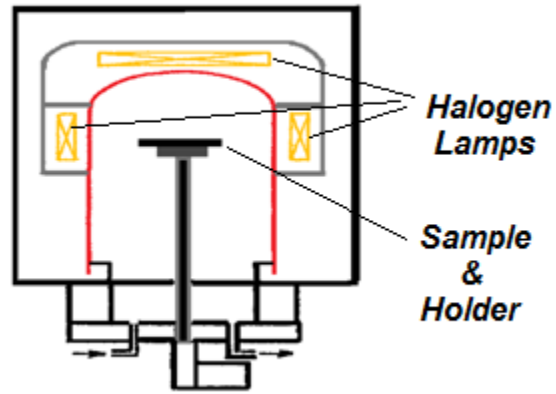


Figure 3.8 Schematics of a RTA furnace

3.6. Metal Induced Crystallization (MIC)

Metal-induced crystallization (MIC) is a new technique to fabricate crystalline Si on glass substrates. In this technique, the temperature of the crystallization can be lower than those for the SPC technique.

3.6.1. Metal Coating Process for Metal Induced Studies

For the process of MIC, one needs to create a thin metal film on the substrate. This metal film can either be used directly or converted to nanoparticles. The a-Si thin film is then evaporated on the metal films for MIC process.

A thermal evaporation system employed for metal coating which shown in Figure 3.9. In this system, the metal pieces placed in a boat which is heated up by passing a high current through the boat. This process fulfill in a chamber with 10^{-4} vacuum level and in room temperature.

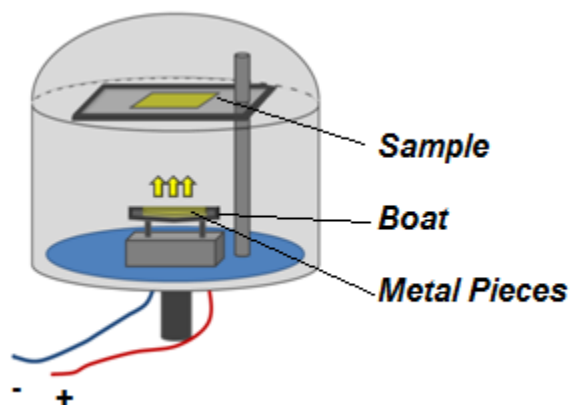


Figure 3.9 Schematics of the thermal evaporator

3.6.2. Metal Induced Crystallization by Au Nanoparticles (AuNPs)

As a substrate, AF 32 Schott glasses with a thickness of 1.1 mm were used. 400 nm of Aluminum doped zinc oxide (AZO) was coated by sputtering technique. For nanoparticle formation, firstly a gold (Au) film with 15 nm was deposited onto AZO film by e-beam method and then the samples were annealed at different temperatures in a classical furnace under N_2 atmosphere. Gold nanoparticles (AuNPs) were imaged by Scanning Electron Microscopy (SEM). After nanoparticle formation, 1 μm thickness of a-Si was deposited by e-beam at a deposition rate of 1 $\text{\AA}/\text{s}$. During the silicon deposition the substrate temperature (T_s) was kept at 200 $^\circ\text{C}$ and the pressure of the vacuum chamber was 5×10^{-7} torr. The samples were annealed between 500 $^\circ\text{C}$ and 600 $^\circ\text{C}$ in N_2 atmosphere for crystallization process. The simple schematic of the fabrication process is shown in Figure 3.10.

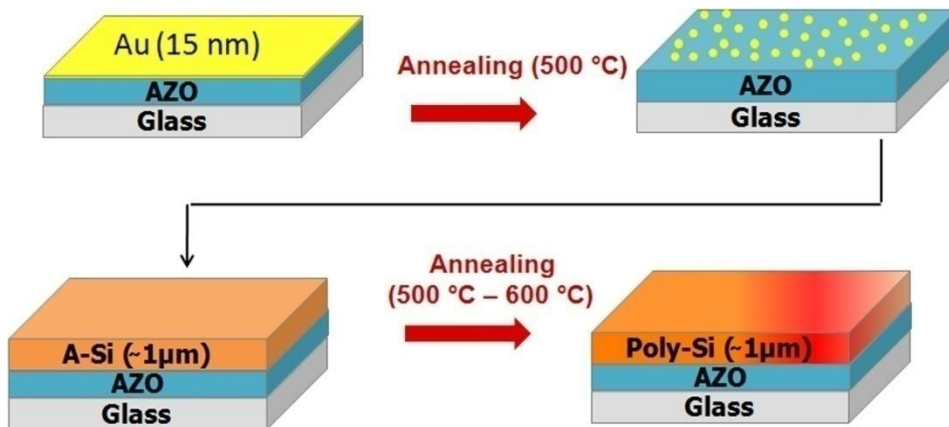


Figure 3.10 Simple schematic of AuNPs induced a-Si crystallization process

3.7. Fabrication of Metal Contacts for Electrical Measurements

Metal contacts for electrical measurements were deposited using a thermal evaporator. In some cases, screen printing technique was used for metal contact formation. The shapes of the metal contacts were defined using shadow masks that were fabricated copper (Cu) sheets as shown in Figure 3.11. For contact to n-type materials silver (Ag) is used, while Al is used for contact to p-type materials.



Figure 3.11 Shadow masks for a) I-V measurements b) Hall effect measurements by van der Pauw technique

3.8. Characterization and Measurement Techniques

In this part of the thesis, we summarize the characterization and measurement techniques. The backgrounds of some optical, electrical and structural measurement methods are briefly given.

3.8.1. I-V Measurements (current vs. voltage)

The electrical properties of the deposited films are crucial for the device operation. Resistivity of the film is the most significant parameter in this manner and it is obtained by measuring the resistance from the surface using a simple configuration as shown in Figure 3.12 below.

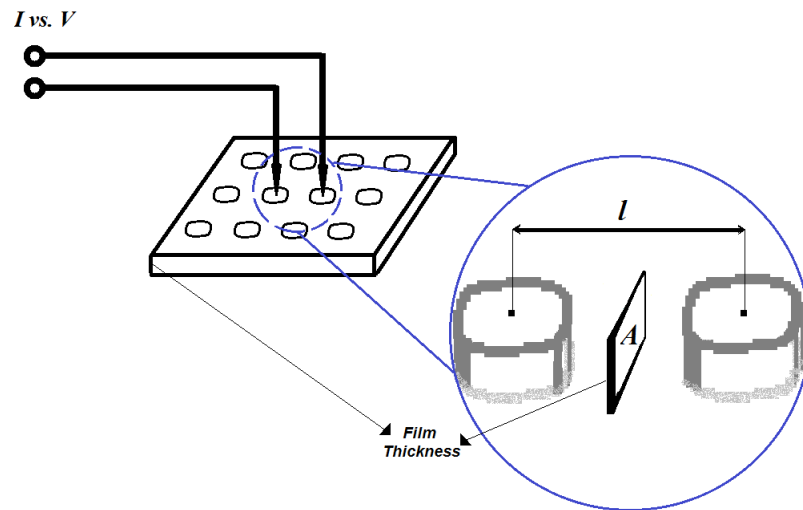


Figure 3.12 Schematics for I-V measurements

By measuring a simple I-V characteristics and using the Ohm's law, $V = RI$, we obtain the resistance between two electrode. The resistivity is then calculated from the formula,

$$\rho = \frac{RA}{l} \quad (3.1)$$

where ρ is the resistivity, R is the calculated resistance, A is the thickness of the film and l is the spacing between the metal contacts.

For I-V measurements a Keithley 2400 Sourcemeter system controlled with Lab View interface was used. The illuminated behavior of the samples was investigated using an Oriol AM1.5G solar simulator available at GÜNAM facility.

3.8.2. Hall Effect Measurements

In semiconductor technology, Hall Effect measurements are commonly used for the determination of carrier mobility, carrier type and concentration. These parameters help us reveal the doping and other impurity effects. In principle, when a current is passed along a sample, the carriers (electrons and holes) are collected at the other two edges in the

presence of a magnetic field which is perpendicular to the current direction. The applied magnetic field generates a voltage across the direction perpendicular to the current direction as a result of the magnetic force acting on the flowing charges. This voltage is called Hall voltage (V_H). The representation of the Hall Effect system is given in Figure 3.13.

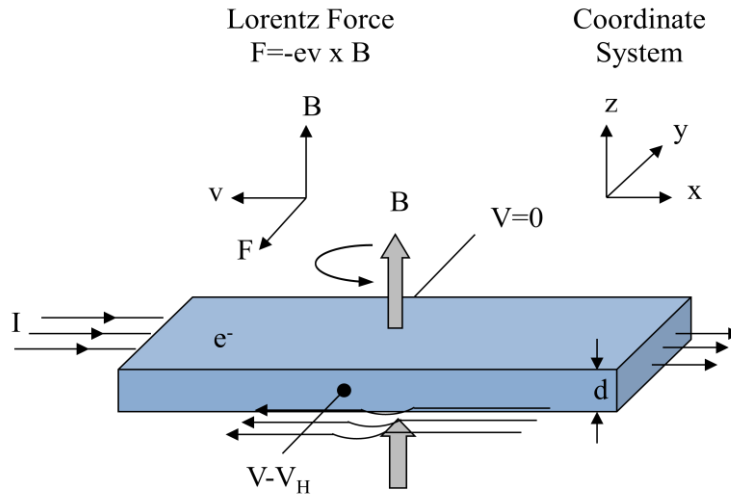


Figure 3.13 Hall Effect Measurement System (for an assumed n-type semiconductor)

In figure 3.13, constant current I (flows along x-axis) in the presence of magnetic field B (z-axis) causes Lorentz force F (y-axis). This causes electron paths to bend towards negative y-axis. Hereby, charge builds up on the surface of the side of sample, and the potential drop across the two sides of the sample is known as the Hall voltage (V_H).

The Hall voltage (V_H) can be written as:

$$V_H = \frac{I_x B_z}{ned} = I_x R_H \frac{B_z}{d} \quad (3.2)$$

The Hall Resistance or Hall Coefficient, (R_H) is often defined:

$$R_H = \frac{1}{ne} \quad (3.3)$$

Then, the hall mobility (μ) can be determined as:

$$\mu = \frac{|V_H|}{R_S I_x B_z} = \frac{1}{R_S n d e} \quad (3.4)$$

For the determination of carrier mobility, measurement begins with forcing both a current perpendicular to the sample and a magnetic field through the product. The Hall voltage (V_H) is then determined. The sample thickness (t) and its resistivity (ρ) are also effective. The resistivity is measured using the same geometry. In this work, so-called van der Pauw sample geometry was used. The resistivity could calculate by Ohm's law. The contact configuration for the mobility and resistivity measurements used in this work are shown in Figure 3.14.

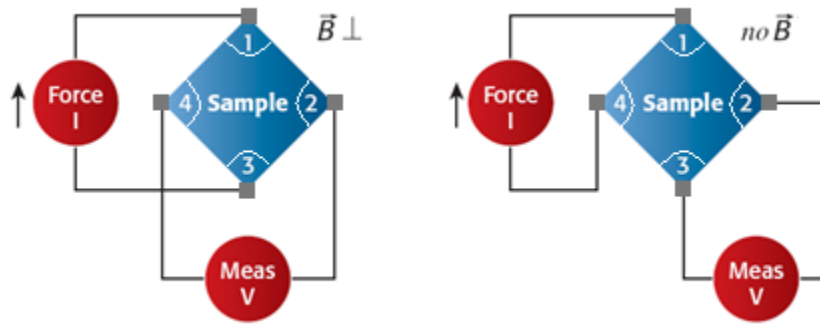


Figure 3.14 Hall Effect voltage vs. van der Pauw resistance measurement configurations.

All the measurements are fulfilled in Atilim Uni. by Lake Shore 7507 Hall Effect measurements system which used to measure the transport resistivity and Hall parameters system.

3.8.3. Time-of-Flight Secondary Ion Mass Spectroscopy

In SIMS (Secondary Ion Mass Spectrometry) analysis, highly energetic primary ions bombard the solid surface. The energy of the primary ion is transported to surface atoms via atomic collisions. As a result of momentum transfer the surface atoms are sputtered away. A simple representation of SIMS analysis is shown in Figure 3.15. Some part of the energy is transferred back to the surface to achieve the surface binding energy. The interaction of the collision cascade with surface molecules is enough to excite even big and non-volatile molecules with masses up to 10,000 u to sputter out without or with little fragmentation.

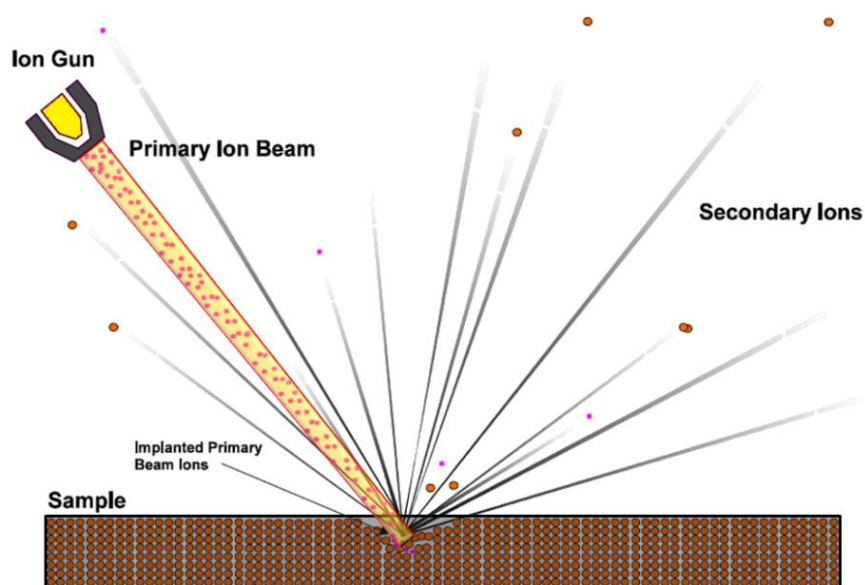


Figure 3.15 Representation of SIMS experiment. Primary beam removes substrate atoms from the surface.

Most of the emitted particles are neutral in charge. However, a small proportion of the charges are positively or negatively charged. The subsequent mass analysis of the emitted ions gives information about the elemental and molecular composition of the surface or even depth profile depending on the sputtering time. All the SIMS measurements were carried out at the Central Lab of METU by *ION-TOF ToF-SIMS 5* system. The schematics of this system is shown in Figure 3.16. This system is composed of an ion gun and a mass spectrometer that analyzes the ions sputtered from the surface.

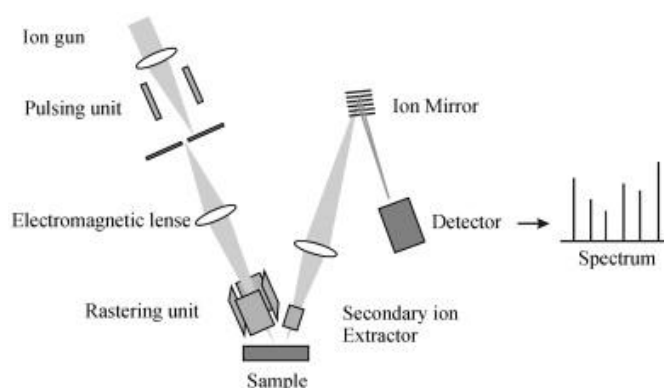


Figure 3.16 Systematics of the ToF-SIMS systems of METU Central Laboratory [65]

3.8.4. Scanning Electron Microscopy (SEM)

In this study SEM is mostly used to image the metal nanoparticles formation. In a conventional SEM system, the energetic electrons are created by an electron gun which can be a field emission or tungsten gun. The electron beam is accelerated by a high voltage on the order of kV to reach the desired energy and passes through a system of apertures and electromagnetic lenses before reaching the sample. The beam is scanned on the surface of the sample, and, secondary electrons emitted from the sample surface are collected by a detector for imaging purposes. All SEM measurements were carried out in the Central Lab of METU by *QUANTA 400F Field Emission SEM* system.

3.8.5. Raman Spectroscopy

Inelastic scattering of a monochromatic light establishes the bases of Raman spectroscopy. Best monochromatic light can be accessible by a laser source. In inelastic scattering, the frequency of monochromatic light is changed through the interaction with the sample. In fact, photons are absorbed once by the sample then reemitted. By originating the original monochromatic frequency of used laser, shifting up and down of the reemitted photons, frequency is monitored. This is named as the Raman Effect. These shifts provide information about vibrational, rotational and other low frequency transitions in molecules. If some part of the energy of the incoming photon is absorbed then it is released with lower frequency with respect to the original state. This is called Stokes frequency. However if the frequency of the reflected photon is increased due to the readily available energy in vibrational states, then this is called Anti-Stokes frequency. If there is no change in frequency between the incoming and reflected photons, this is called Rayleigh scattering which stands for most of the photons. Figure 3.17 simply shows the three situations.

In this study, a confocal micro-Raman, HR800 Jobin Yvon was employed at GÜNAM Measurement Laboratory. This system includes attachments of an Olympus microanalysis system and a charge-coupled device (CCD) camera providing a resolution of 1 cm^{-1} . The spectra were carried out in backscattering geometry with He-Ne laser's 632.8 nm line at room temperature. Since, all cases measured at the same detailed conditions, all results and Raman peaks are comparable.

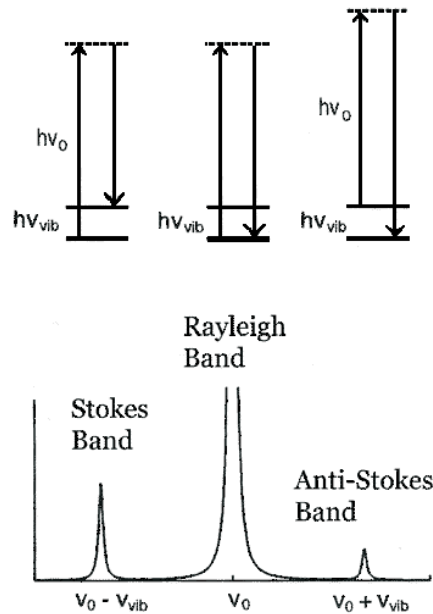


Figure 3.17 Shift up and down in Raman Spectra [66]

3.8.6. X-Ray Diffraction Measurement (XRD)

X-ray diffraction is capable of giving information about the atomic arrangement in solids. In diffraction case, an X-ray wave is reflected from regularly spaced atomic planes. The beam reflected from different atomic planes form destructive and constructive diffraction patterns which are used to extract the information about the distance between the atomic planes. The schematic of X-ray diffraction experiment is shown in Figure 3.18.

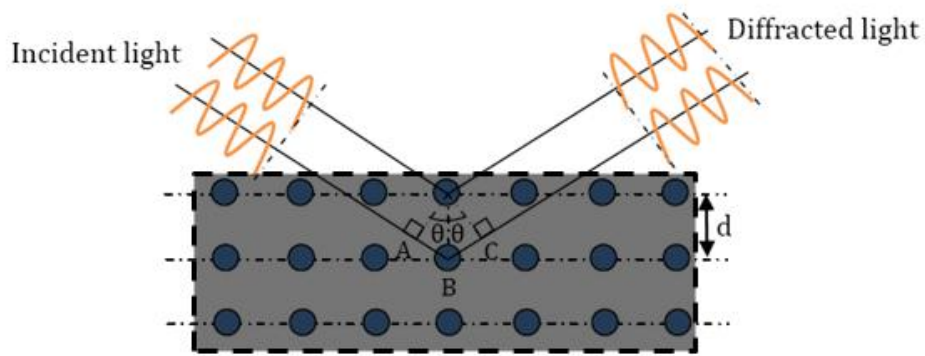


Figure 3.18 Schematics of the X-Ray Diffraction experiment

The well known diffraction condition is given by the expression

$$n\lambda = 2d\sin\theta \quad (3.5)$$

where n stands for an integer number, θ shows the angle and d is the interatomic spacing. All the XRD measurements were made by Mini Rigaku X-Ray diffractometer at GÜNAM Measurement Lab.

CHAPTER 4

RESULTS AND DISCUSSION

In this chapter, we present the results of our studies on crystallization and doping of thin films by e-beam evaporation. As described in the previous chapters, fabrication of thin film crystalline Si on glass substrate might lead to revolutionary developments in the cost of solar energy. The crystallinity of Si improves the electronic transport, and carrier life-time for an efficient charge collection. In order to reach this aim, various approaches have been implemented in different laboratories. Most of these studies focus on the low temperature crystallization of Si on ordinary glass substrates. Low temperature is necessary because the glass softens at about 600 °C and any crystallization attempt should use temperatures below this value. Unfortunately, Si does not crystallize at temperatures below 600 °C. Solution of this dilemma will create a significant contribution to the developments in the thin film crystalline research. In this chapter, we present two approaches: one is the control of the crystallization by evaporation rate; the second approach is metal induced crystallization by metal nanoparticles. Both of these approaches aim to lower the crystallization temperature without lowering the crystal quality.

4.1. Crystallization of a-Si Thin Films Prepared by e-beam Evaporation

Crystallization of a-Si deposited by evaporation or other techniques on glass substrates can be induced by SPC process, which has been commonly used in many laboratories for the fabrication of solar cells [50]. However, it is known that crystallization of Si takes place at around 600 °C, which is critical for the use of ordinary glass. Many research groups have used prolonged annealing up to 30 hours to obtain the crystal formation at this critical temperature [50].

In order to overcome the temperature problem, crystallization with the help of metal catalysts has been investigated. In this approach, very low level crystallization could be obtained at very low temperatures. Below, we give our results both on SPC and metal induced crystallization. We also discuss the effect of ZnO substrate on the crystallization.

4.1.1. Solid-Phase Crystallization (SPC)

The SPC technique relies on the nucleation of crystallization in the bulk of a-Si and grain growth on these crystal sites by a diffusion process. Models on the crystallization have been discussed in Chapter 2.

Figure 4.1 shows the Raman spectra for a-Si film annealed at 750 °C for different annealing durations up to 15 h. We clearly see the transition from the amorphous to crystalline phase. The as-deposited sample exhibits a broad peak at 490 cm⁻¹, which is typically observed from a-Si.

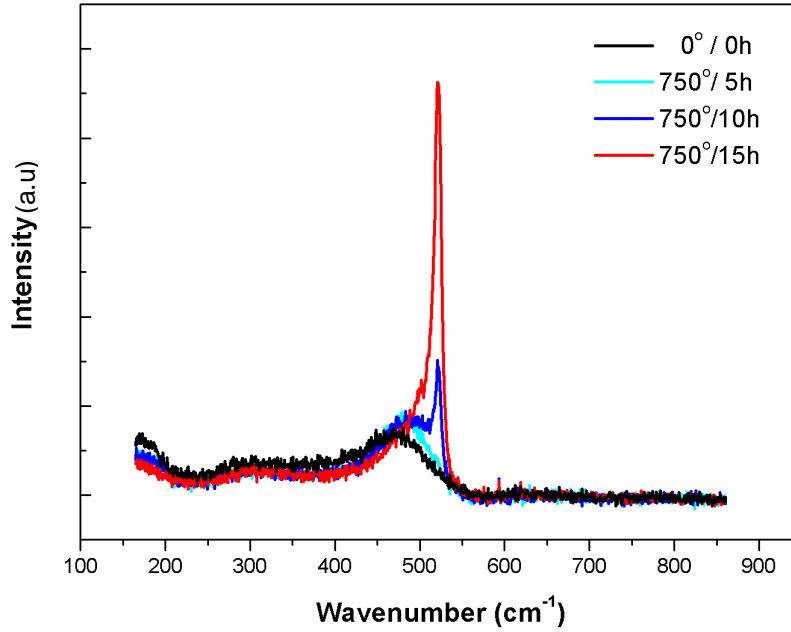


Figure 4.1 Study of *a*-Si model sample [500 nm thick, 10 Å/s deposited on AF32[®] eco glass substrate at 200 °C] annealed at 750 °C in different time wholes

Although some shift to higher wave numbers are seen, no significant variation is observed in the shape of the *a*-Si peak for the annealing durations up to 10 h. The overall crystallinity of the film can be determined from the Raman peaks through the analysis of the peaks corresponding to deconvolution of crystalline peaks from the amorphous ones. For this purpose, different signals comprising the observed main peak at 523 cm⁻¹ should be resolved by a deconvolution process. We used the software program called Peak Fit to obtain the peaks shown in Figure 4.1. Following this deconvolution process, the amount of crystallization can be calculated by the following expression [67]

$$x_c = \frac{I_c + I_i}{I_c + I_i + I_a} \quad (4.1)$$

where I_a , I_i and I_c are the integrated Raman intensities corresponding to the amorphous phase, intermediate phase and the crystalline phase, respectively.

The amount of crystallization is plotted against the annealing time in Figure 4.2. It seems that the rate of crystallization increase after some time. This is clearly related to the onset of crystal nucleation in the amorphous matrix. Once the nucleation starts the crystal grains grow more rapidly. This is in agreement with the previous studies on the crystallization process.

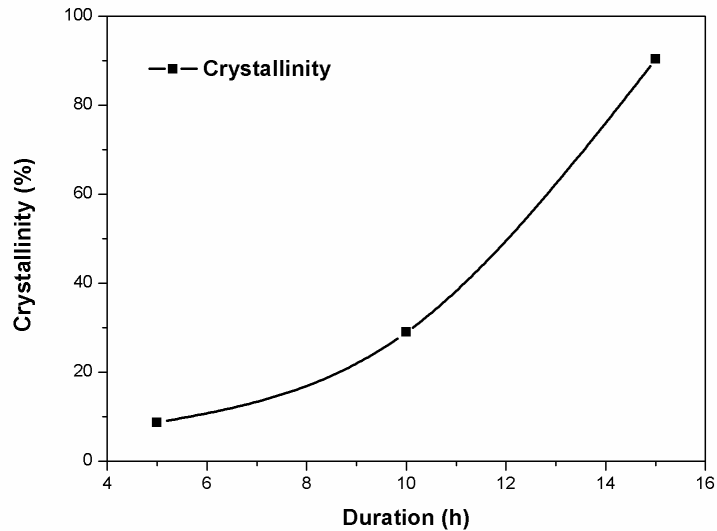


Figure 4.2 Crystallinity changes vs. annealing time

4.1.1.1. Effect of evaporation rate on the crystallinity

It is known that the crystallization process starts with nucleation and continues with a growth on the nucleated sites by a diffusion process. It is highly dependent on the process temperature and the time. We can then expect a dependence on the evaporation rate especially when the substrate is heated. In this case, some nucleation at the nanoscale can be initiated even during the growth if the atoms are given sufficient time to diffuse. So we might expect a higher crystallinity for the lower evaporation rates. We have carried out a series of experiments to investigate this dependence. Table 4.1 shows the samples prepared at different rates and processed under different experimental conditions. Note that we used RTA in this case.

Table 4.1 Naming the sample through conditions on deposition rate, thickness and RTA temperature

Sample name	Dep. Rate (A/s)	Estimated Thickness(nm)	RTA Temp.
1	20	500	As-deposited
2	5	500	As-deposited
3	20	250	As-deposited
4	5	250	As-deposited
11	20	500	800°C-10min
21	5	500	800°C-10min
31	20	250	800°C-10min
41	5	250	800°C-10min
51	1	500	800°C-10min
61	50	500	800°C-10min
13	20	500	800°C-15min
23	5	500	800°C-15min
53	1	500	800°C-15min
63	50	500	800°C-15min

Figure 4.3 and 4.4 show the Raman spectra of the samples evaporated at four different rates and annealed at 800 °C for 10 min and 15 min, respectively. We see that the crystallinity of the films is very sensitive to the evaporation rate. The crystallization starts only when the evaporation rate is below a certain threshold value. Although it might be expected intuitively, this effect has not been reported previously. The rate effect can be better understood with the model based on the nucleation-diffusion process, which previously discussed in Chapter 2 of this thesis work.

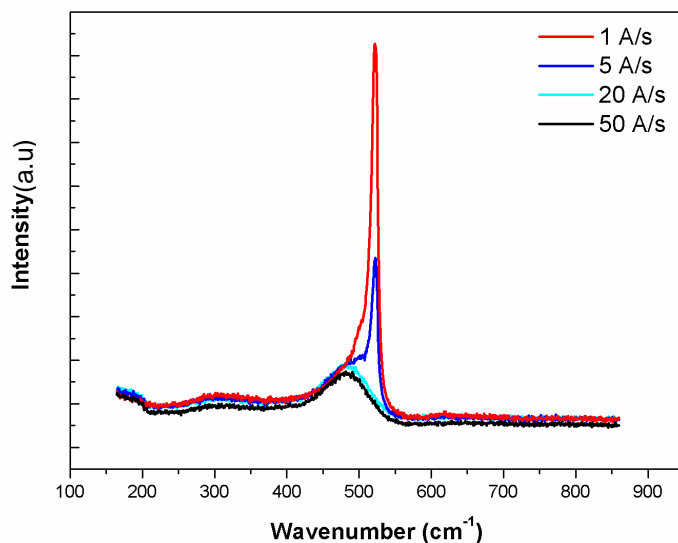


Figure 4.3. Crystallization study by getting deposition rate as only variable in 800 °C-10min annealing case

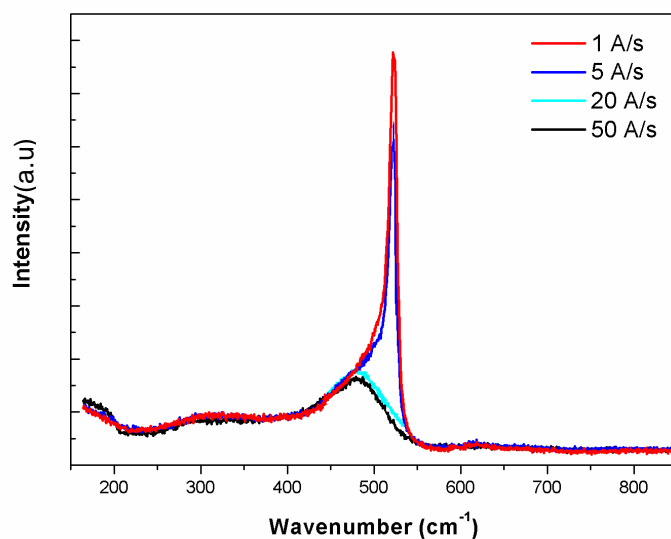


Figure 4.4 Crystallization study by getting deposition rate as only variable in 800 °C-15min annealing case (5 min more)

4.1.1.2. Effect of film thickness on the crystallinity

The crystallization always starts with a nucleation which might also depend on the film thickness. We know from the micro-crystalline silicon ($\mu\text{-Si}$) grown by PECVD that the micro crystal film growth following the deposition of a certain amount of film has take place. In order to check whether we have a similar effect in the e-beam evaporated films, we have studied the crystallinity with the film thickness. Figure 4.5 compares two evaporation rates with two different film thicknesses. The crystallization starts after a critical film thickness and the effect of the films thickness is drastically seen at low deposition rates. The crystallinity increases with the film thickness as might be expected from the PECVD studies.

This can be understood easily with the same model developed for the $\mu\text{-Si}$ growth as described by previously in Chapter 2. The structure of the film expected from this model had schematically shown in Figure 2.1.

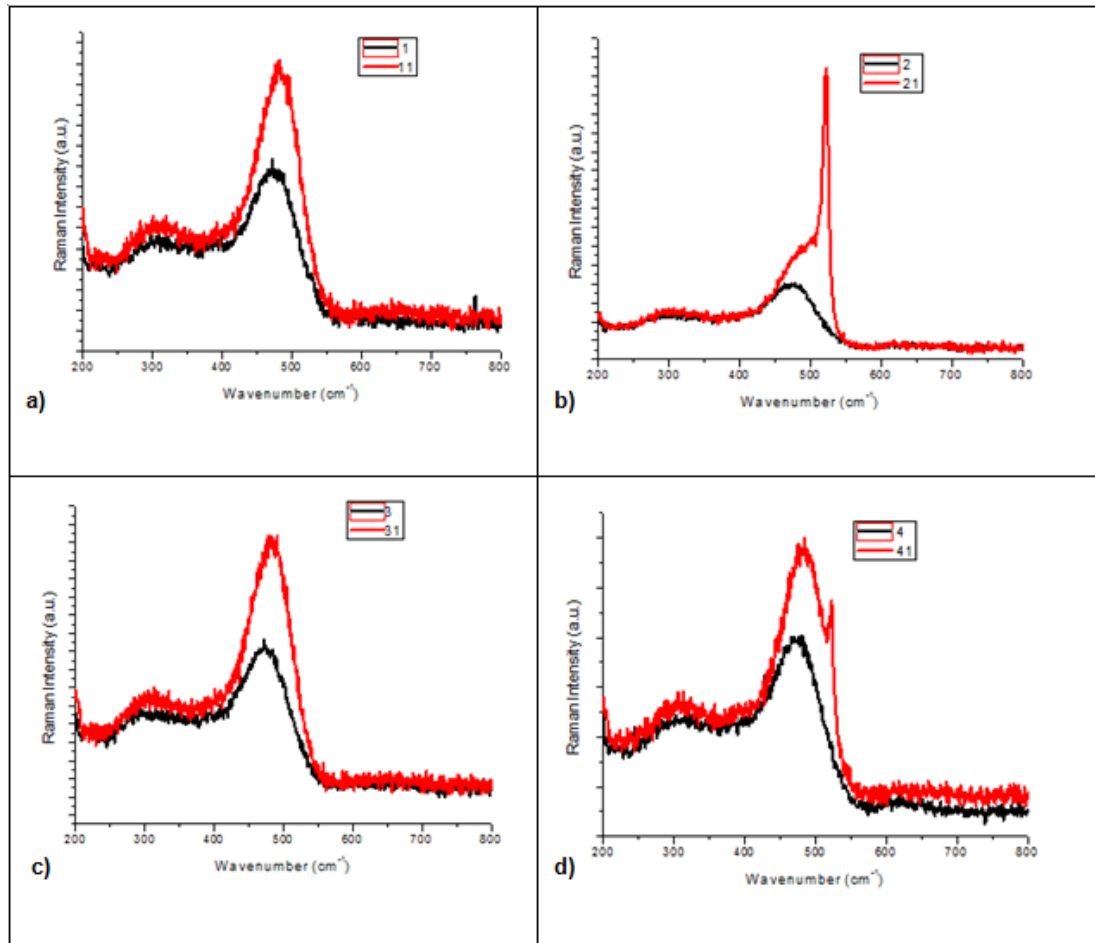


Figure 4.5 Comparison of thickness and deposition rate effect on crystallization amount; a) 20 A/s & 500 nm, b) 5 A/s & 500 nm, c) 20 A/s & 250 nm and d) 5 A/s & 250 nm

4.1.1.3. Effect of substrate: SPC on Al doped ZnO (AZO)

In this section we present the results of our study on the effect of crystallization on the substrate materials. The effect can be twofold: the surface properties of the substrate, such as roughness, thermal conductivity, mobility of the atoms and molecules, etc. can retard or enhance the crystallization of the Si film. To see these effects, we studied the crystallization on the AZO substrate. The Raman results of the films deposited on AZO substrate are shown in Figure 4.6. These samples were annealed exactly under the same experimental conditions with those displayed in Figure 4.1. In this case, the crystallization started a shorter annealing duration compared to those on the glass substrate.

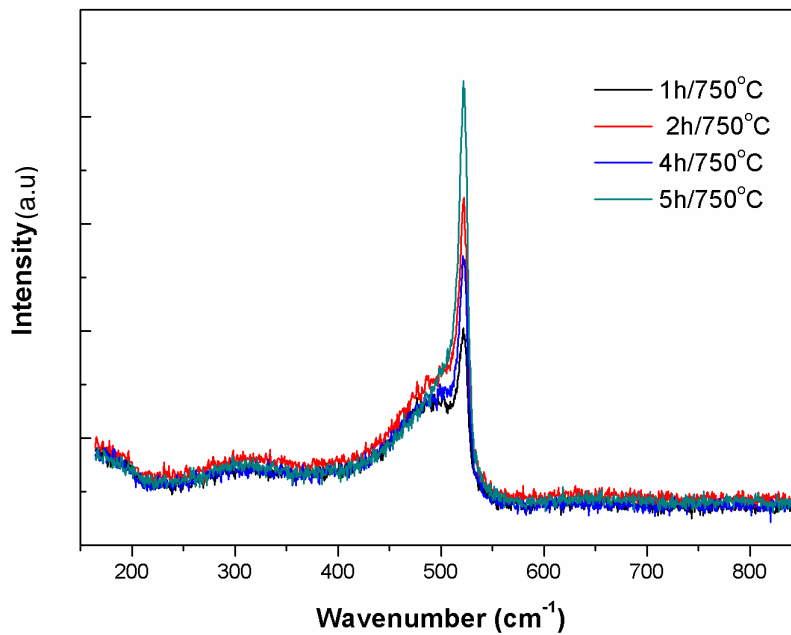


Figure 4.6 Study of a-Si model sample [500nm thick, 10 A/s deposited on 400nm AZO coated AF32[®] eco glass substrate at 200 °C] annealed at 750 °C in different time whiles

So, the presence of the AZO substrate enhances the crystallization process. This effect can be explained by two effects: the surface mobility of the Si atoms adsorbed on the surface is higher on AZO surface than on glass substrate. So the nucleation of the crystallization starts on the AZO substrate at the very early stage of the deposition which may helped by AZO rough surface, too. The second reason might be the Al atoms present in the AZO film can act as the catalyst for the nucleation of the crystallization. It is not clear which one of these mechanisms is more effective at this stage. More detailed investigation is needed to clarify this point.

4.1.1.4. Effect of e-beam spot size (current density) on the film properties

In e-beam evaporation process, the electron beam is focused on the source material, i.e., Si in the present case. When the evaporation rate is kept constant, the size of the e-beam spot might affect the film properties. This is because the local heat generated by the e-beam depends on the beam current density at the point of the e-bam strike. In order to grow a-Si film by a narrow spot, one should apply a high e-beam current (e.g. 230 mA for 50 A/s)

which results in the same deposition rate of wider spot with lower e-beam current (e.g. 100 mA for 50 A/s). This difference in the beam current generates a different temperature distribution in the chamber and in the evaporated Si atoms leading to differences in the structure of the deposited film. In Figure 4.7 the Raman spectra shows that wider spot lead to starting the crystallization in 650 °C annealing for 1 hour much more effective than narrower spot's sample.

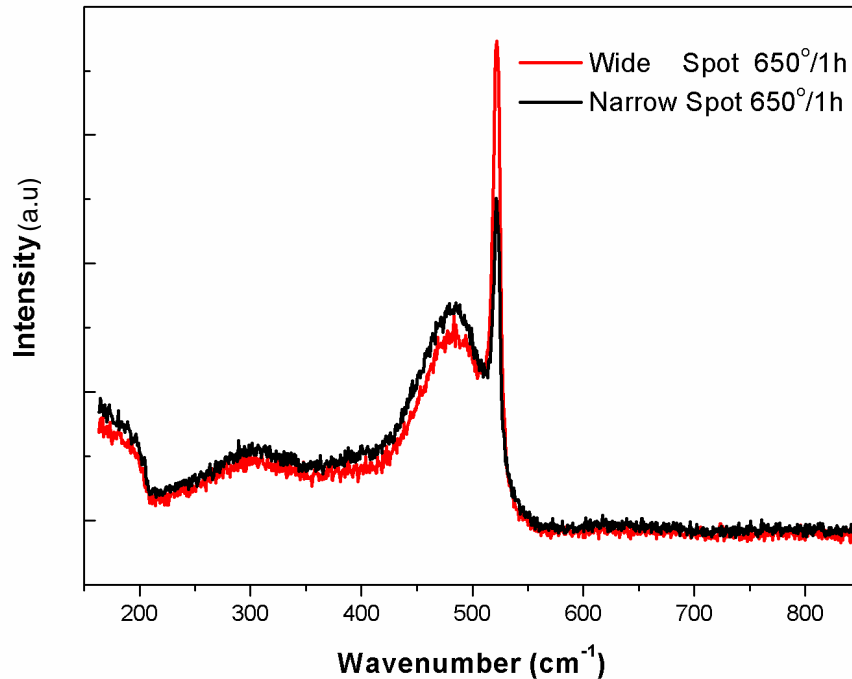


Figure 4.7 Comparison of two spot shape results in 650 °C annealing for 1 h which is a kind of threshold annealing for 1000nm 50A/s deposited a-Si sample

4.1.2. Metal Induced Crystallization by Au Nanoparticles (AuNPs)

MIC has been used to enhance the crystallization process with get the essential annealing temperature to a lower degree. An introduction and a short review on this technique are given in Chapter 2. Here, we report on the use of metal nanoparticles (NP) instead of continuous thin film, which because of its distribution; it is expected to generate less metal contamination than conventional MIC using continuous metal films. The e-beam evaporated Au film (~15 nm) on AZO film (~400 nm) was annealed to obtain AuNPs and the best nanoparticles in terms of uniformity and size was obtained by annealing at 500 °C for 1 hour. The SEM image of the AuNPs is shown in Figure 4.8. As it is seen in this figure, most of the AuNPs' sizes are between 50 nm and 150 nm. The size distribution of NPs is affected by the initial Au film thickness. The thinner films resulted in smaller and more agglomerated NPs. In this situation, since the metal NPs act as nucleation centers, the resulting silicon grain size will be larger with more widely spaced NPs.

In Figure 4.9, the Raman results from the samples with AuNPs that were annealed at 500 °C, 550 °C and 600 °C for 12 h are given. As it is clear from this figure that the amorphous structure is maintained for the sample annealed at 500 °C. The crystallization starts by annealing at 550 °C and the film substantially crystallizes at 600 °C for the same period of time.

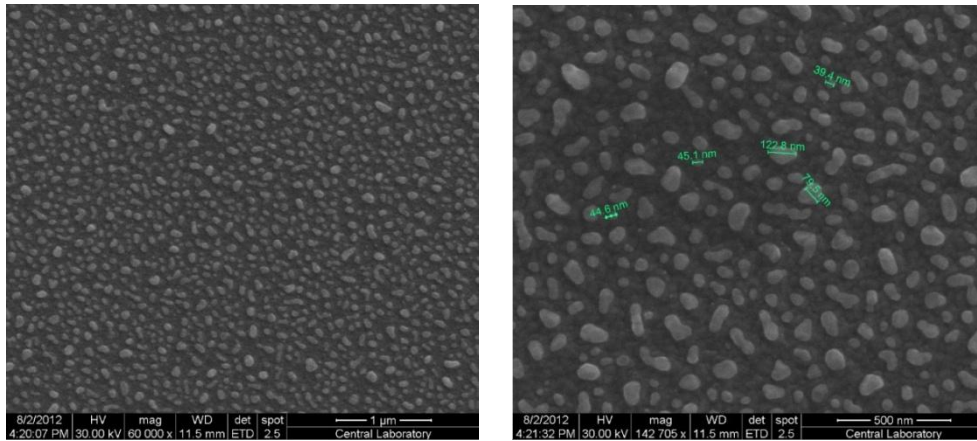


Figure 4.8 SEM images of 15 nm gold thin film after annealing at 500 °C for 1 hour

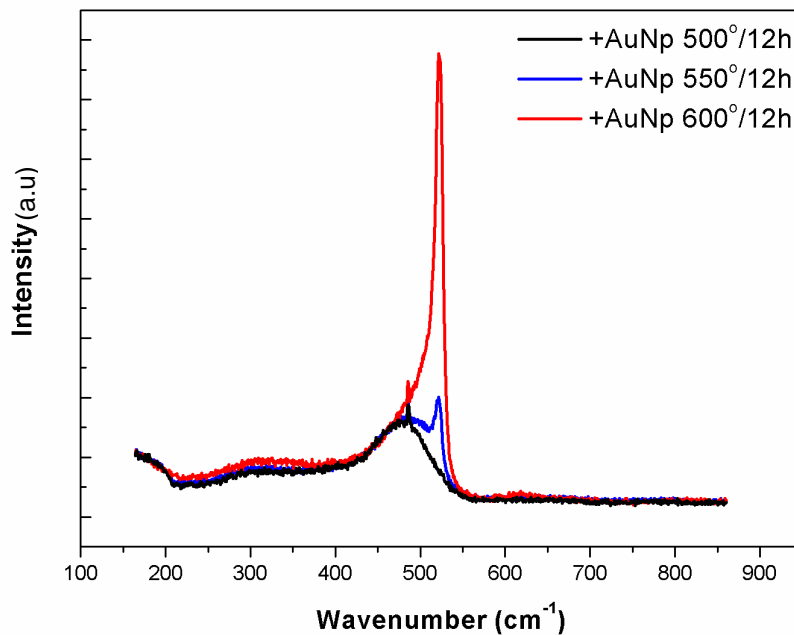


Figure 4.9 Raman measurements for samples of 1 µm - 1 Å/s a-Si with AuNPs on AZO/glass substrate annealed for 12 h at 500 °C, 550 °C and 600 °C

Results presented above show that the crystallization starts at temperatures as low as 500 °C and reaches a high fraction at 600 °C. In order to find out if the crystallization can

occur in a shorter time interval, we performed the same experiments for an annealing time of 12 h at 600 °C. Results are shown in Figure 4.9.

XRD results obtained from the same samples are shown in Figure 4.10. We see that the crystalline silicon orientations of <111>, <220> and <311> are clearly detected in the samples annealed at 600 °C. In the samples annealed at lower temperatures, <111> peak is observable, while the others are almost invisible. <111> peak is strongest in the XRD spectrum since it has the lowest free energy [67][68]. The approximate crystalline grain size in the grown film was analyzed by the Scherrer equation [69],

$$D = \frac{K \cdot \lambda}{\beta \cdot \cos\theta} \quad (4.2)$$

where D is the average grain size, K is the Scherrer's constant, λ is the X-ray wavelength (1.542 Å), β is the full width at half maximum (FWHM) of the peak and θ is the Bragg angle. The calculated average crystalline grain size from <111> peak for the sample annealed at 600 °C for 12 h is 15.6 nm.

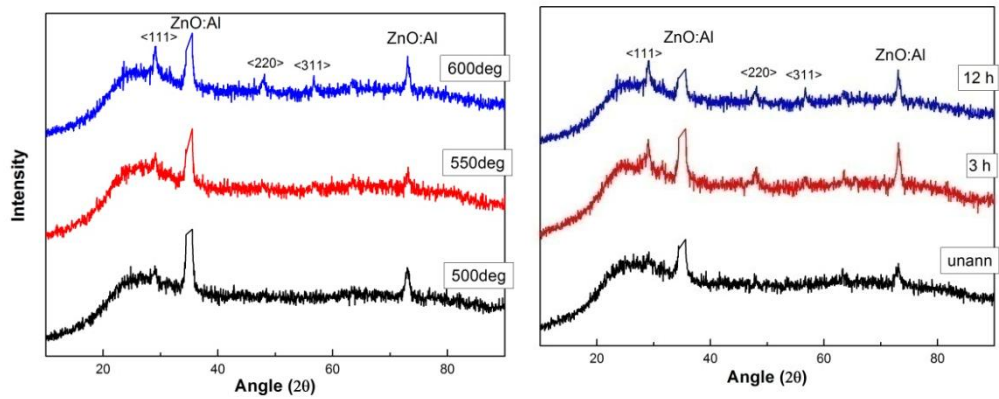


Figure 4.10 XRD measurements for samples of 1 μm - 1 $\text{\AA}/\text{s}$ a-Si with AuNPs on AZO/glass substrate annealed for 12 h at 500 °C, 550 °C and 600 °C, also at 600 °C for 0 h, 3 h, 12 h

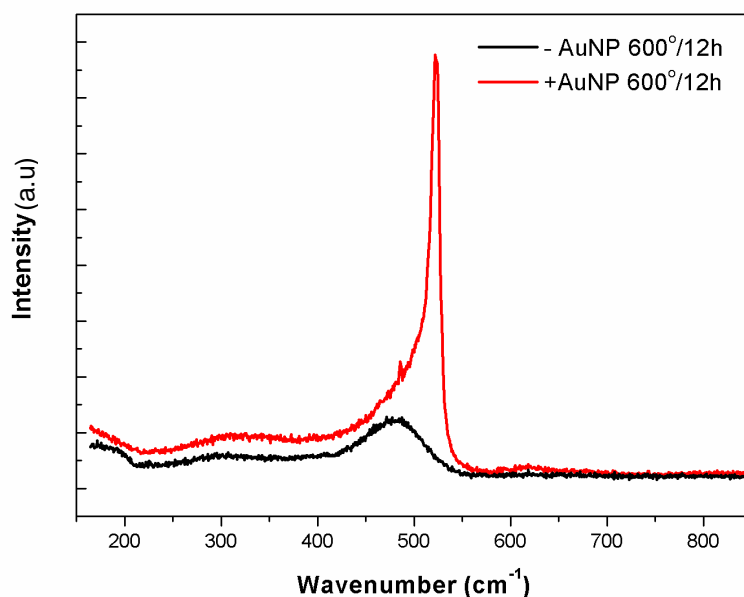


Figure 4.11 Effect study of AuNPs for case of 600 °C annealing for 12 h

The Raman results of the samples with and without AuNPs annealed at 600 °C for 12 h are given in Figure 4.11. As seen, the AuNPs induce the crystallization in 3 h, while the sample without gold nanoparticle has no crystallization even after 12 h annealing. Crystallization in a short time like 3 h is attractive when compared to classical SPC method. It is obvious that as the annealing time increases, the crystallinity increases. However, 3 h the annealing is still giving acceptable crystallinity with respect to 12 h annealing.

As mentioned before, to calculate crystallinity amounts (X_c), deconvoluted Raman spectra was used. The calculated crystalline amounts are given in Table 4.2.

Table 4.2 Crystallinity amounts of AuNPs induced samples with respect to different annealing temperature and time

Annealing Temperature (°C)	Annealing Time (h)	Crystallinity Amounts (%)
500	12	amorphous
550	12	25
600	3	66
600	12	73

The results in the table show that the crystallinity amount increases by both time and temperature. Besides, there is no considerable difference between the crystalline amounts of the samples annealed at 600 °C for 3 h and 12 h.

We have shown that metal nanoparticles considerably enhance the crystallization. As an important advantage, the use of less metal introduces less contamination to the grown film. This technique deserves to be investigated in a more detailed and systematic way.

4.2. Doping a-Si Thin Film Deposited by e-beam Evaporation

Doping is crucially important for the solar cell production. As described in Chapter 2, both p and n type doping are necessary to fabricate the p-i-n structures, which constitutes the typical solar cell structure. For n and p type doping P and B elements are used, respectively. The e-beam evaporation system we used in this study is equipped with two effusion cells with B and P sources. It is; however, not straightforward to achieve doping. As tabulated in Table 4.3, we have fabricated 6 samples of P and B doped and analyzed them using SIMS and electrical techniques.

Table 4.3 Effusion cells' temperature survey study table

Effusion cell temperature for P	Effusion cell temperature for B
600 °C	1700 °C
700 °C	1800 °C
800 °C	1900 °C

4.2.1. SIMS Results

We have deposited 500 nm a-Si film with in-situ doping. The SIMS results are shown in Figure 4.12 and 13 for these samples. Unfortunately, SIMS results are not quantitative because of lack of the reference sample. As a quantitative analysis, we can only make comparisons among the same type of samples. SIMS data show, however, that we have successfully doped the layers with P and B as we expected. The dependence of dopant concentration on the effusion cell temperature is as expected for the boron case, i.e., the amount of dopant increases with the increasing cell temperature. However, for the case of P doping we observe a reverse relationship, i.e., the dopant concentration decreases with increasing cell temperature. The reason for this reverse relation is not clear to us at this point. Since the absolute differences between SIMS signals are not known the degree of the differences could not be estimated. It is likely that the differences between the actual values are very small.

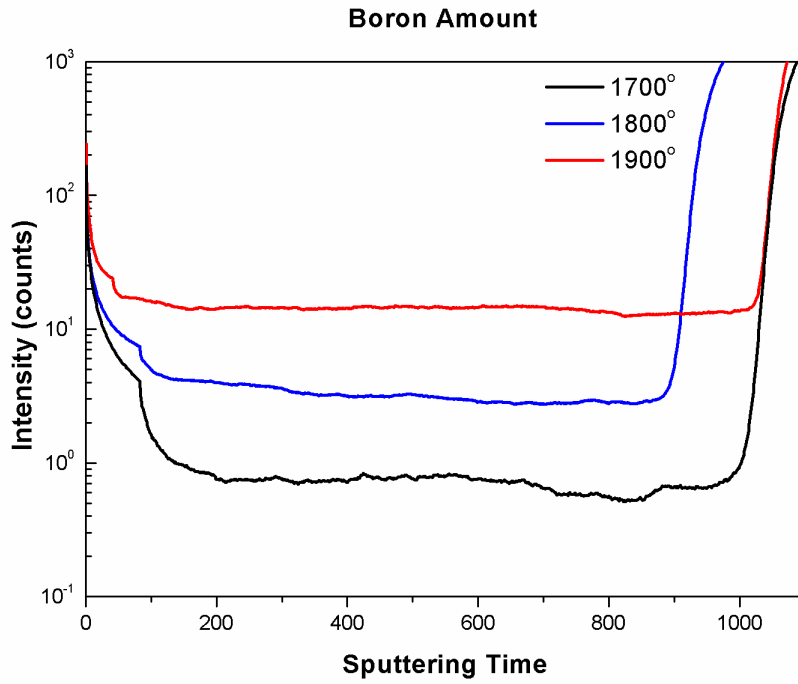


Figure 4.12 SIMS result of B doping in effusion cell's different temperatures

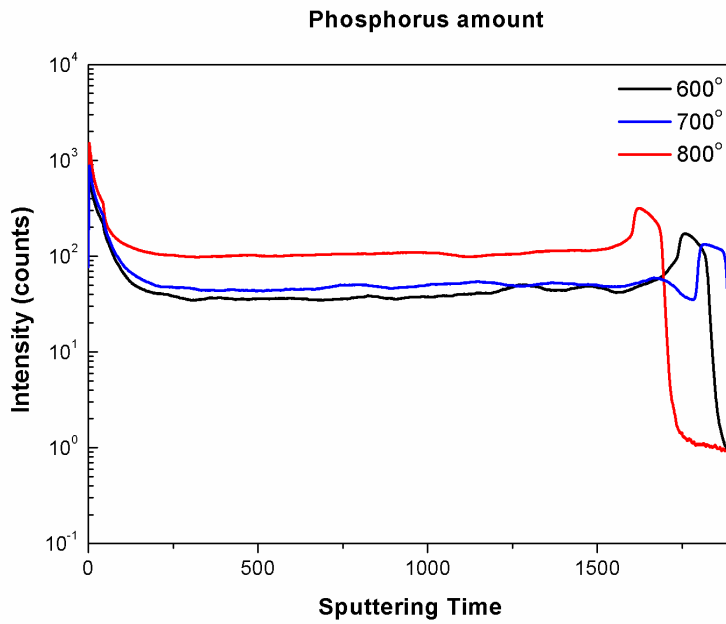


Figure 4.13 SIMS result of P doping in effusion cell's different temperatures

4.2.2. Electrical measurements

We have performed both I-V and Hall Effect measurements on the fabricated amorphous samples. Generally, the resistivity of the as deposited a-Si films is very high, in many cases it is not measurable. We expect significant reduction in the resistivity upon doping process. In Figure 4.14 and 15, we show the variation of I-V curves with doping. We observe that the current voltage characteristics are linear, indicating the presence of an ohmic contact between the metal contacts and the Si film.

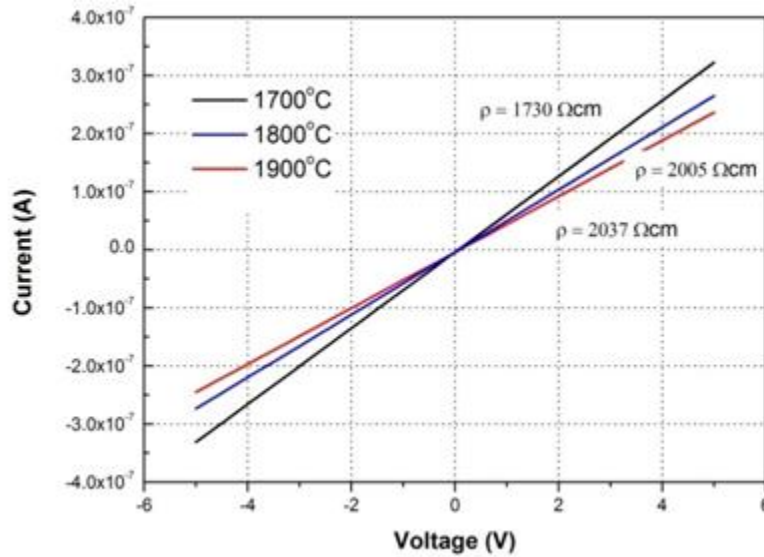


Figure 4.14 I-V curve for Boron doping of different effusion cell temperatures

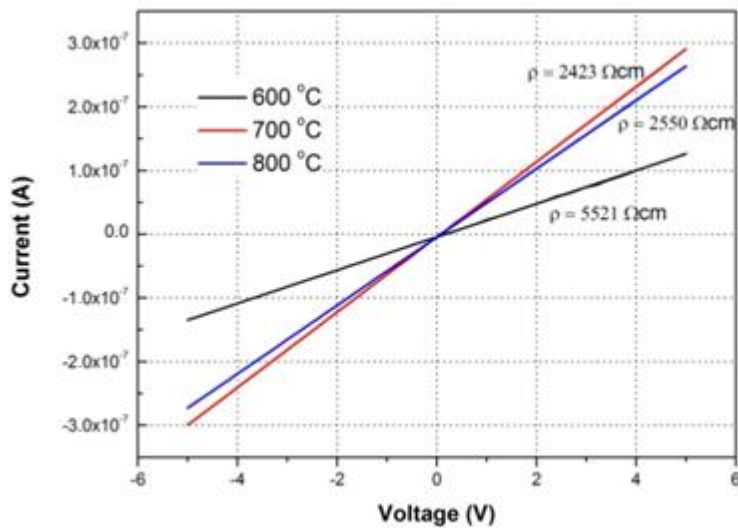


Figure 4.15 I-V curve for Phosphorous doping of different effusion cell's temperatures

For boron doping, the I-V plot of effusion cell temperatures 1800 °C and 1900 °C brings much higher resistivity. However temperature of 1700 °C results in lower resistivity

For Phosphorous doping, the I-V plot of effusion cell temperatures 600 °C and 800 °C brings much higher resistivity. However temperature of 700 °C results in lower resistivity.

The resistivity values calculated from these curves have consistency with the values which would presume in the Table 4.4. As shown in this table, the resistivities are high compared to the values reported in the literature which dedicated before in chapter 2.

We have also performed Hall Effect measurements on the samples reported above. The results of the resistivity and Hall Effect are shown in Table 4.4 and 5.

Table 4.4 Hall Effect measurements for B-doped samples with different effusion cell temperatures

B Doped	Resistivity [Ω cm]	Hall Coefficient [cm ³ /C]	Carrier Density [1/cm ³]	Hall Mobility [cm ² /(V.s)]
1700 °C	1.71E+03	2.33E+02	2.67E+16	1.44E-01
1800°C	2.02E+03	1.30E+03	4.80E+15	7.58E-02
1900 °C	2.24E+03	5.08E+02	1.22E+16	5.49E-02

Table 4.5 Hall Effect measurements for P-doped samples with different effusion cell temperatures

P Doped	Resistivity [Ω cm]	Hall Coefficient [cm ³ /C]	Carrier Density [1/cm ³]	Hall Mobility [cm ² /(V.s)]
600 °C	5.50E+03	7.32E+02	8.52E+15	1.26E-03
700 °C	2.43E+03	1.20E+02	5.22E+16	4.49E-02
800 °C	2.50E+03	4.60E+02	1.35E+16	1.90E-01

Although, the highest dopant concentration amount in SIMS results seems to be for the sample doped with 1900 °C effusion cell temperature, the Hall Effect measurements indicate that the amount of active carriers is highest for the sample doped with B and P with 1700 °C and 700 °C effusion cell temperature. The origin of this result could be the dopants

nanoclusterization (agglomeration of some dopant atoms) due to excess amount of dopant atoms.

4.2.3. Activation energy measurement

Here, by the aid of a cryostat, we have measured the conductivity through 60-300 K. By plotting them as below the activation energy (E_a) is achievable (Figure 4.16 and 17).

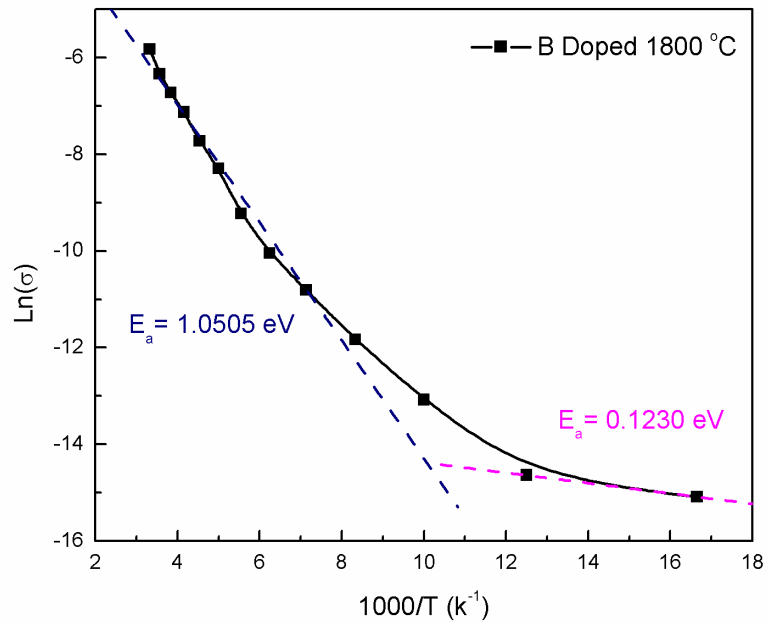


Figure 4.16 Activation energy measurement for B-doped sample

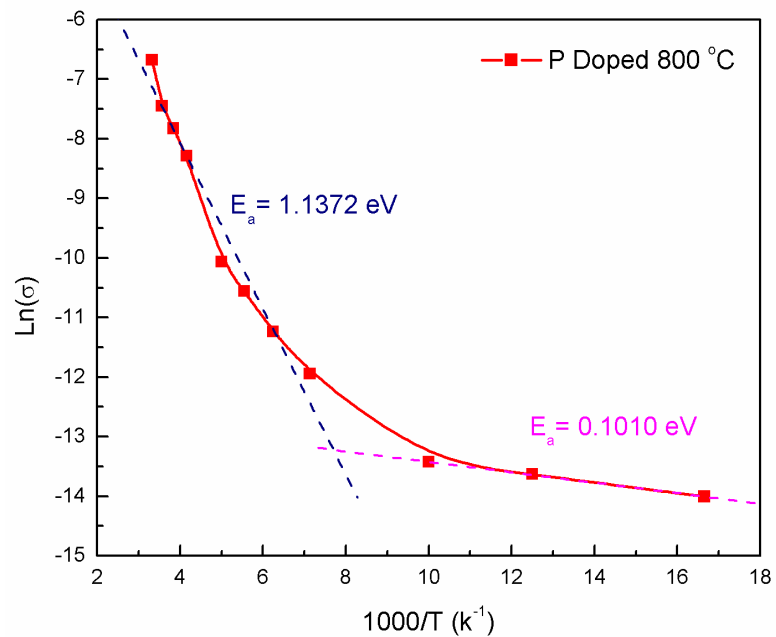


Figure 4.17 Activation energy measurement for p-doped sample

Activation Energy released from:

$$E_a \text{ eV} = \frac{\ln \sigma}{\frac{1000}{T}} \cdot \frac{1000k_B}{q} \quad (4.3)$$

which $\ln(\sigma) / (1000/T)$, equals to the slope, k_B is Boltzmann constant and q is the carrier charge in eV.

We have performed conductivity measurements as a function of the temperature as shown in Figures 4.16 and 4.17 for B and P doped samples respectively. We identify two distinct regions with quite different activation energies in each sample. The activation energies were measured to be 1.05 eV and 1.13 eV in the high temperature region and 0.12 eV and 0.10 eV in the low temperature region of the $\ln(\sigma)$ vs. $1/T$ plots of the B and P doped samples respectively. These results indicate two regimes for the conductivity, which is a function of the carrier density. The number of charge carriers depends on the excitation from the valence band or impurity state to conduction band. At low temperatures, the low activation energy corresponds to the energy required to excite an electron (hole) from the impurity state created by the dopant atoms. This energy is called impurity ionization energy. The measured values (0.12 eV and 0.10 eV) are in agreement with the foreseen values [70]. In a crystalline bulk Si crystal, the impurity ionization energy is around 20-40 meV which is much smaller than what is found here. The difference is due to the larger band gap of a-Si.

The high activation energy corresponds to excitation process from the valence band to the conduction band of the a-Si. In c-Si these values should be roughly equal to the half of the band gap energy (0.56 eV). In the present case, the band gap energy is around 1.7 eV, which should yield activation energy of 0.85 eV. The measured values are higher than this value. The reason might be the position of the defect state that helps the excitation process. If the defect state is not located at the midgap, the activation energy could be higher than the half of the band gap energy.

4.3. Contamination from the glass substrate

4.3.1. SIMS Results

The contamination caused by the impurity diffusion from the glass substrates which contain various unwanted impurities had studied and summarized as the impurity analysis that performed in the Si film by SIMS and XRF analysis. SIMS profiles obtained from the Si film presented in Figure 4.18. The impurities observed in the film are shown below.

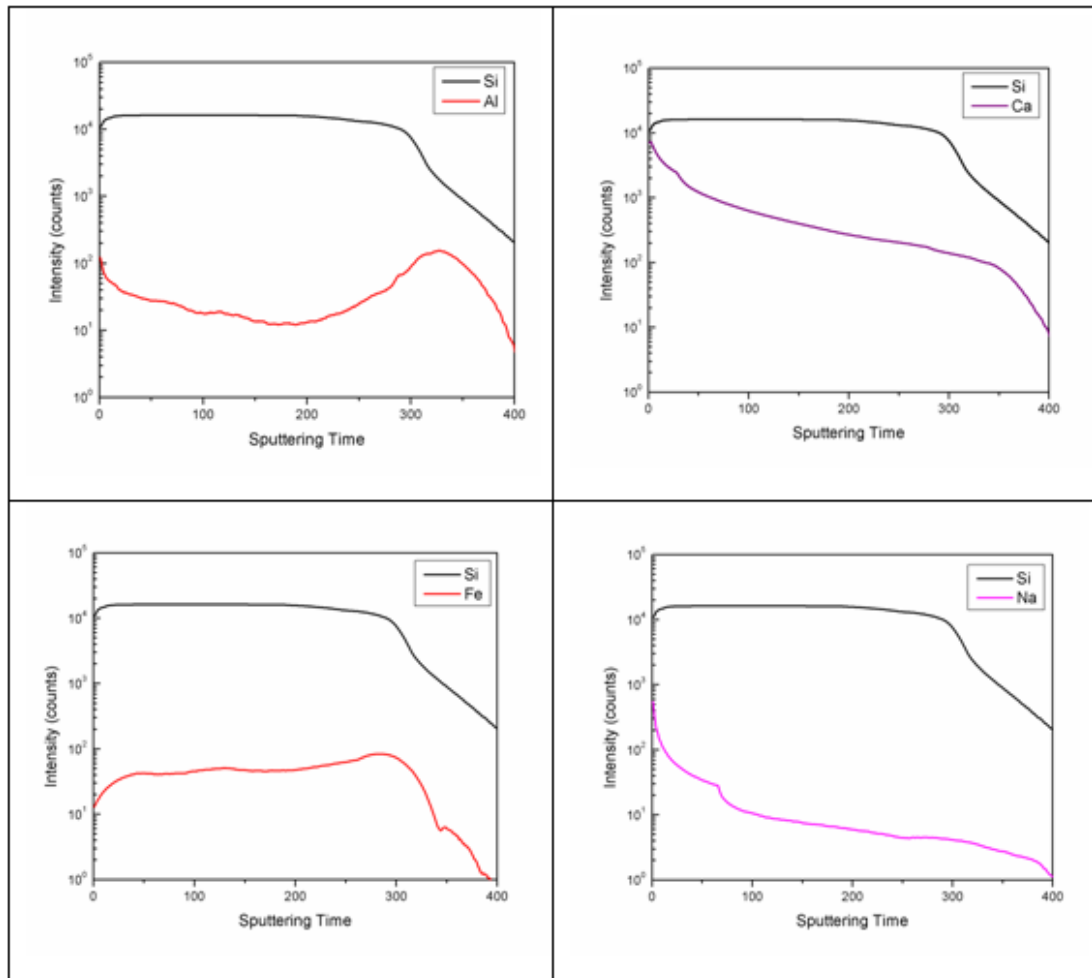


Figure 4.18 SIMS result to compare Al, Ca, Fe and Na impurities in a-Si film

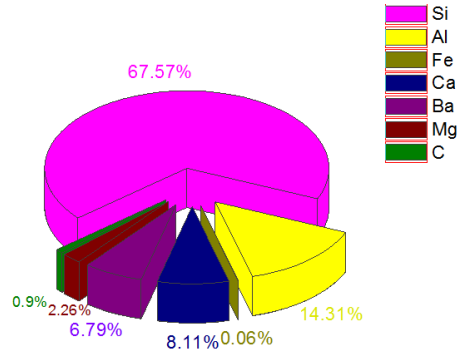
4.3.2. XRF Results

To understand the origin of this contamination, we analyzed the chemical structure of the film and glass by XRF and seen that the glass is the main source of contamination. For a quantitative survey the XRF spectroscopy was employed. Results are presented in Figure 4.19.

As future works, in order to prevent this contamination we suggest covering the glass substrate with Si_3N_4 , which would act as a good diffusion barrier for impurities.

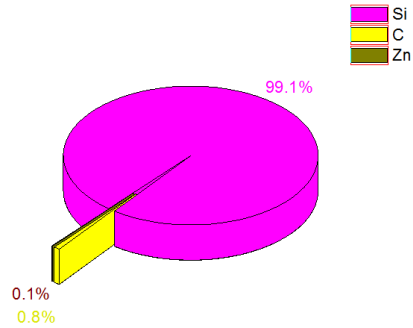
a-Si on Glass

Component	Re. Mass%
Si	46.4
Al	9.83
Fe	0.04
Ca	5.57
Ba	4.66
Mg	1.55
C	0.62



a-Si on Si wafer (as reference)

Component	Re. Mass%
Si	99.1
C	0.8
Zn	0.1



Bare Glass

Component	Re. Mass%
SiO ₂	58.30
Al ₂ O ₃	17.90
B ₂ O ₃	8.70
Fe ₂ O ₃	0.02
Ca	3.53
Ba	2.76
Mg	1.82

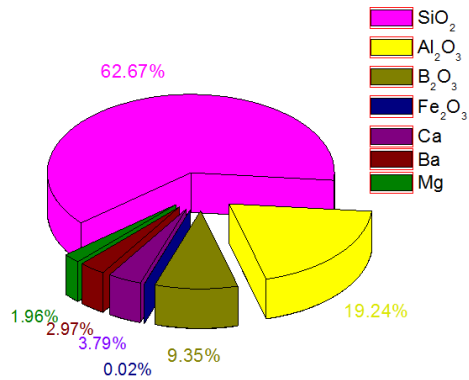


Figure 4.19 XRF Results

CHAPTER 5

CONCLUSIONS

The photovoltaic technologies are becoming more and more important as the environmental, economical, and political problems created by the use of fossil fuels for the energy demand of the world are growing around the globe. The climate change caused by the CO₂ emission resulted from the fossil fuel burning is threatening the future. It is then inevitable to replace the conventional energy sources (oil, gas and coals) by clean and renewable energy sources. Among the renewable energy sources, solar energy is the only source with the largest abundance, cleanness and accessibility from everywhere around the world.

Photovoltaic (PV) technologies are widely used to convert the solar energy to electricity. It has been recognized as an important alternative to all other energy producing technologies. PV industry today is dominated by the crystal Si based solar cells with a market share of 90%. c-Si cells have high conversion efficiency, are proven to be robust, and reliable for a very long time (up to 30 years). However, c-Si based solar cells suffer from high production costs that make the competition with other energy sources very difficult. Although the price fall we have observed in recent years has made them very attractive in many locations in the world, their price is still higher than the price of the electricity generated by natural gas and coal for a real competitive position for them.

In searching cost effective and more efficient alternative solutions, new and different PV technologies have been developed. Thin film solar cells have been a major breakthrough in the history of PV technologies. Among the thin film systems, a-Si/ μ c-Si systems have attracted attention due to the same reason as the c-Si systems (robustness, durability, abundance). a-Si thin film solar cells can be fabricated on glass or stainless steel substrates with very large area (up to 5.7 m²). With less material usage, a-Si/ μ c-Si thin film technology offers a low cost solution. However, the efficiency has been much lower than the c-Si solar cells. The maximum stable efficiency of this type of solar cells has been around 10%, which is almost half of the efficiency of c-Si solar cells.

In order to combine the efficiency advantages of c-Si and cost advantage of the thin film system, significant amount of efforts have been devoted for fabrication of crystalline thin films on glass substrates. However, this is a challenging issue due to the fact that crystallization of Si without a seed does not yield a single crystal. Moreover, the temperature of crystallization is higher than the softening temperature of the glass substrates. These difficulties have made the crystallization of Si quite challenging. Many research groups around the world have been trying to obtain highly crystalline thin film layers on glass substrate at low temperatures.

In this M.Sc. thesis study, we have investigated the fabrication of thin film crystalline Si on glass by e-beam evaporation followed by an annealing process either in a conventional tube furnace or in a RTA system. Some of the produced films were doped with P and B using effusion cells integrated to the e-beam evaporator.

Upon annealing at temperatures above 600 °C, we have observed crystallization in the a-Si thin film as expected. The crystallization increases with the annealing temperature and duration as expected. Interestingly, we have observed a strong dependence of the crystallization on the evaporation rate. We obtained higher crystallinity in the samples deposited with slower rates. This is understandable because, when the evaporation rate is low, atoms arriving at the surface will have more time to reach a crystallization site for the nucleation and growth. We have also observed that the crystallization depends on the thickness of the film. Thickness dependence is typically observed in the crystal formation in the a-Si films produced by PECVD. Another interesting and positive effect is observed when the film is deposited on ZnO film, which is the case in the solar cell device fabrication. ZnO provides either higher mobility for the atoms arriving at the surface, or Al atoms that enhance the crystallization just like metal induced crystallization we summarized below.

We have studied metal induced crystallization using metal nanoparticles instead of continuous film. We expect lower crystallization temperature and lower contamination in this case. We have shown that when Au nanoparticles are incorporated, crystallization starts at temperatures as low as 500 °C and reaches to very high fractions at 600 °C. So, the total annealing time is reduced significantly in this case. However, the contamination by the metal nanoparticles is still not identified. We need to investigate the effect the contamination on the material and device properties in the future.

Doping has been accomplished using effusion cells incorporated to the e-beam evaporation system. We have observed the expected variation with the doping process. The resistivity decreases with the doping in general. We have also determined the doping type and carrier concentration as a function of effusion cell temperature and doping type. In most of the cases, we have observed right conductivity type. For some samples annealed at relatively high temperatures, the doping type was measured to be inconsistent with the expected results. This is attributed to the contamination from the glass substrate. To understand the origin of this contamination, we analyzed the chemical structure of the film -on glass and on Si wafer (as reference) - and glass itself by XRF and seen that the glass is the main source of contamination. In order to prevent this contamination, we suggest covering the glass substrate with Si_3N_4 which would act as a good diffusion barrier for impurities.

We finally studied the temperature dependent I-V characteristics of the films. We have observed two distinct regions with two activation energies at high and low temperatures. These regions correspond to two different current mechanisms. One of the mechanisms (low temperature one) is likely to be driven by the generation of carriers through band tails stated in the a-Si, and the other one (high temperature) is determined by the barriers in the conduction band. The conduction in the amorphous or nano-, and micro-crystalline Si thin film is a complicated process, and full understanding of the conduction requires very detailed investigation. This will be an important task in our future studies.

REFERENCES

- [1] "WORLD ENERGY OUTLOOK 2012", INTERNATIONAL ENERGY AGENCY (IEA)
- [2] "KEY WORLD ENERGY STATISTICS", INTERNATIONAL ENERGY AGENCY (IEA)
- [3] A.E. Becquerel, Comt. Rend. Acad. Sci. 9 (1839) 561
- [4] "APPARATUS FOR UTILIZING SOLAR RADIANT ENERGY", Patent US389124
- [5] "The Nobel Prize in Physics 1921: Albert Einstein", Nobel Prize official page
- [6] K. A. Tsokos, "Physics for the IB Diploma", Fifth edition, Cambridge University Press, Cambridge, 2008, ISBN 0-521-70820-6
- [7] <http://oai.dtic.mil/oai/oai?verb=getRecord&metadataPrefix=html&identifier=AD0419878>, last accessed on 10.02.2013
- [8] Perlin (1999) p. 50
- [9] "Solar: photovoltaic: Lighting Up The World retrieved" 19 May 2009
- [10] "Solar Stocks: Does the Punishment Fit the Crime?" (FSLR, SPWRA, STP, JASO, TSL, LDK, TAN) – 24/7 Wall St. 24/7 Wall St. (2011-10-06). Retrieved on 2012-01-03.
- [11] "BP Statistical World Energy Review 2011" (XLS). Retrieved 8 August 2011
- [12] http://www.c2es.org/technology/factsheet/solar#_edn37, last accessed on 10.02.2013
- [13] <http://www.pveducation.org/pvcdrom/solar-cell-operation/efficiency>, last accessed on 10.02.2013
- [14] L.L. Kazmerski, J. Electron Spectrosc. Relat. Phenom. 150 (2006) 105–135
- [15] <http://rredc.nrel.gov/solar/spectra/> [U.S. Department of Energy: Description of Air-Mass], last accessed on 10.02.2013
- [16] Gueymard, C. Solar Energy, Volume 76, Issue 4, April 2004, Pages 423-453.
- [17] Solar Photovoltaics, RENEWABLE ENERGY TECHNOLOGIES: COST ANALYSIS SERIES Vol.1 Issue 4/5 Jun2012.–
- [18] M. A. Green. "Third generation photovoltaics: solar cells for 2020 and beyond", Physica E, 14:65–70, 2002.
- [19] W.Chen, B. Sopori, , "Photovoltaics for the 21 st Century, Proceedings of the Electrochemical Society International Symposium", Kapur, V. K., et al., eds., May 1999, Seattle, p. 145, Washington. Electrochemical Society Proceedings Vol. 99- 11(1999).
- [20] Y. Zhao, X. Jiang, W. Wang, Z. Li, Y. Yu and X. Liao, Proceedings of Twenty Sixth IEEE Photovoltaic Specialist Conference —1997, p.569. (Anaheim, CA, September, 1997).
- [21] Y. Zhao, X. Jiang, W. Wang, Z. Li, Y. Yu and X. Liao, Proceedings of Twenty Sixth
- [22] IEEE Photovoltaic Specialist Conference —1997, p.569. (Anaheim, CA, September, 1997).
- [23] M.D. Efremov et al, Proc. SPIE, 2801, p. 263 (1996).
- [24] M. A. Green. "Photovoltaics: technology overview." Energy Policy, 28:989– 998, 2000.
- [25] K. Yamamoto, A. Nakajima, M. Yoshimi, T. Sawada, S. Fukuda, T. Suezaki, M. Ichikawa, Y. Koi, M. Goto, T. Meguro, T. Matsuda, M. Kondo, T. Sasaki, and Y. Tawada. "A high efficiency thin film silicon solar cell and module." Solar Energy, 77:939–949, 2004.
- [26] http://www.mse.mtu.edu/~pearce_images_proto2.jpg, last accessed on 10.02.2013
- [27] M.L. Hitchman and K.F. Jensen. "Chemical Vapor Deposition." Academic Press, 1993.
- [28] B. Loisel, L. Haji, and M. Guendouz. "LPCVD silicon for active devices." Journal de Physique (Colloque), 1989.
- [29] F.R. Faller, V. Henninger, A. Hurrle, and N. Schillinger. "Optimization of the CVD process for lowcost crystalline-silicon thin-film solar cells." In 2nd World Conference on PV Solar Energy Conversion, Vienna, page 1278, 1998.
- [30] R. Rogel, K. Kis-sion, T. Mohammed-Brahim, M. Sarret, O. Bonnaud, and J.P. Kleider. "High quality LPCVD polycrystalline silicon films in solar cell applications." In 2nd World Conference and Exhibition on Photovoltaic Solar Energy Conversion, Vienna, 1998.
- [31] T. Mohammed-Brahim, K. Kis-sion, D. Braind, M. Sarret, and O. Bonnaud. "Towards large grain size and high thickness polycrystalline silicon lms for silicon solar cells." In 13th European Photovoltaic Solar Energy Conference, Nice, 1995

- [32] E. Conrad, L. Elstner, W. Fuhs, W. Henrion, P. Müller, J. Poortmans, B. Selle, and U. Zeimer. "Low-temperature homoepitaxy of silicon by electron cyclotron resonance CVD." In 14th European Photovoltaic Solar Energy Conference, Barcelona, 1997.
- [33] Ritsuko Iiduka, Akira Heya, and Hideki Matsumura. "Study on cat-CVD poly-Si films for solar cell application." *Solar Energy Materials and Solar Cells*, 48, 1997.
- [34] A.R. Middy, J. Guillet, J. Perrin, A. Lloret, and J.E. Bouree. "Hot-wire chemical vapour deposition of polycrystalline silicon films." In 13th European Photovoltaic Solar Energy Conference, Nice, 1995.
- [35] J.K. Rath, H. Meiling, and R.E.I. Schropp. "Low-temperature deposition of polycrystalline silicon thin films by hot-wire CVD." *Solar Energy Materials and Solar Cells*, 48, 1997.
- [36] J. Cifre, J. Bertomeu, J. Puigdollers, M.C. Polo, J. Andreu, and A. Lloret. "Polycrystalline silicon films obtained by hot-wire chemical vapour deposition." *Applied Physics A*, 1994.
- [37] H.N. Wanka, M.B. Schubert, A. Hierzenberger, and V. Baumung. "Prospects of microcrystalline silicon from hot-wire CVD for photovoltaic applications." In 14th European Photovoltaic Solar Energy Conference, Barcelona, 1997.
- [38] A. Breymesser, V. Plunger, M. Ramasori, V. Schlosser, M. Nelhiebel, P. Schattschneider, D. Peiro, C. Voz, J. Bertomeu, and J. Andreu. "Investigations of polycrystalline silicon layers deposited by hot wire CVD." In 2nd World Conference and Exhibition on Photovoltaic Solar Energy Conversion, Vienna, 1998.
- [39] J. Meier, J. Sitznagel, U. Kroll, C. Bucher, S. Fay, T. Moriarty, A. Shah, *Thin Solid Films* 451–452 (2004) 518
- [40] A.V. Shah, J. Meier, E. Vallat-Sauvain, N. Wyrsh, U. Kroll, C. Droz, U. Graf, *Solar Energy Materials and Solar Cells* 469–491, (2003)
- [41] M. A. Green, K. Emery, Y. Hishikawa, W. Warta, *Prog. Photovolt: Res. Appl.* 2011; 19:84–92
- [42] M. J. Keevers et al, 22nd European PV Conf, Milan, 2007, p1783
- [43] S. Gall et al, Solar-TR2, Antalya, Turkey, Oral Presentation
- [44] J. Schneider, A. Schneider, A. Sarikov, J. Klein, M. Muske, S. Gall, W. Fuhs, "Aluminum-induced crystallization: Nucleation and growth process." *J. Non-Crystalline Solids* 352 (2006) 972–975
- [45] B. Pécz, L. Dobos, D. Panknin, W. Skorupa, C. Lioutas, N. Vouroutzis. "Crystallization of amorphous-Si films by flash lamp annealing." *App. Surface Science* 242 (2005) 185–191
- [46] A.T. Voutsas. "A new era of crystallization: advances in polysilicon crystallization and crystal engineering." *App. Surface Science*, 208–209 (2003) 250–262
- [47] Ch. Chou, D. Wu, R. Yan, F. Chou, "Low-Temperature Metal Induced Crystallization of Amorphous Silicon Using Nano-Nickel Particles." *J. Solid Mechanics and Materials Engineering*, 5 (2011) 25–32
- [48] Z. Tan, S.M. Heald, M. Rapposch, C.E. Bouldin, J.C. Woicik, "Gold-induced germanium crystallization." *Phys. Rev. B*, 46 (1992) 9505.
- [49] O. Nast, T. Puzzer, L. M. Koschier, A. B. Sproul, and S. R. Wenham. "Aluminum-induced crystallization of amorphous silicon on glass substrates above and below the eutectic temperature." *Appl. Phys. Lett.*, 73(22):3214.
- [50] Ö. Tüzün, "Polycrystalline Silicon Films by Aluminium Induced Crystallization and Epitaxy: Synthesis, Characterizations and Solar Cells", PhD Thesis. Université de Strasbourg 2009
- [51] D. D. Malinowska, O. Angelov, M. Kamenova, M. S. Vassileva, "Polycrystalline silicon thin films obtained by metal-induced crystallization." *J. Mater. Sci: Materials in Electronics*, 14 (2003) 747–748
- [52] T. N. Nguyen, V. D. Nguyen, S. Jung, J. Yi, "The metal-induced crystallization of poly-Si and the mobility enhancement of thin film transistors fabricated on a glass substrate." *Microelectronic Eng.* 87 (2010) 2163–2167
- [53] M. Seibt, S. Buschbaum, U. Gnauert, S. W. D. Oelgeschlager, *Phys. Rev. Lett.* 1998, 80, 774.
- [54] L. Pereira, H. Águas, E. Fortunato, R. Martins, "Metal Induced Crystallization: gold versus aluminum." *J. Materials Science*, 40 (2005), 1387–1391.
- [55] A.E. Kolmogorov. "On statistic theory of crystallization of metals." *Izv. Akad. Nauk SSR Ser. Fiz. Mat. Nauk*, 1:355, 1937. original title translated from Russian.

- [56] W.A. Johnson and R.F. Mehl. "Reaction kinetics in processes of nucleation and growth." Trans. Am. Inst. Min. Metall. Pet. Eng., 135:416–442, 1939.
- [57] M. Avrami. "Kinetics of phase change. i.", J. Chem. Phys., 7:1103–1112, 1939.
- [58] M. Avrami. "Kinetics of phase change. ii.", J. Chem. Phys., 8:212–224, 1940.
- [59] M. Avrami. "Granulation, phase change, and microstructure." J. Chem. Phys., 9:177–184, 1941.
- [60] M. Castro, F. Dominguer-Adame, A. Sanchez, and T. Rodriguez. "Model for crystallization kinetics: Deviations from kolmogorov-johnson-mehl-avrami kinetics." Appl. Phys. Lett., 75(15):2205–2207, 1999.
- [61] C. Sagui and M. Grant. "Theory of nucleation and growth during phase separation." Phys. Rev. E., 59(4):4175–4187, 1999.
- [62] "Nucleation and growth during the formation of polycrystalline silicon thin films", PhD Thesis. J. M. Schneider, Technischen Universität Berlin 2005
- [63] http://www.schott.com/special_applications/english/products/thinglass/af32/index.html, last accessed on 10.02.2013
- [64] http://www.schott.com/hometech/english/download/brochure_borofloat_e.pdf, last accessed on 10.02.2013
- [65] M. Saleem, H. Galla, Biomembranes, Vol.1798, Issue 4, (2010), P 730-740
- [66] http://131.104.156.23/Lectures/CHEM_207/vibrational_spectroscopy, last accessed on 10.02.2013
- [67] J. K. Kim, S. J. Yun, J. W. Lim, S. H. Lee, "Effect of deposition conditions and crystallinity of substrate on phase transmission of hydrogenated Si films" J. The Electrochemical Soc. 158 (2011) D430-D434
- [68] T.L. Alford, P.K. Shetty, N.D. Theodore, N. Tile, D. Adams, J.W. Mayer, "Nanocrystalline Si formation in the a-Si/Al system on polyimide and silicon dioxide substrates." Thin Solid Films 516 (2008) 3940
- [69] Z. X. Zhao, R. Q. Cui, F. Y. Meng, B. C. Zhao, H. C. Yu, Z. B. Zhou, "Nanocrystalline silicon thin films prepared by RF sputtering at low temperature and heterojunction solar cell." Mater. Lett. 58 (2004) 3963
- [70] N.F. Mott, Philos. Mag. 19 835 (1969)